aerospace

MDPI

Article

Numerical Study on the Aerodynamic Performance of a UAV S-Shaped Inlet with Grilles

Shu Yang [1], Mingshuang Shi [2], Dongpo Li [3], Zhenlong Wu [1,*], Huijun Tan [1], Jiahao Ren [1] and Liming Yang [4]

[1] College of Energy and Power Engineering, Nanjing University of Aeronautics and Astronautics, Nanjing 210016, China
[2] Association for Science and Technology, Nanjing University of Aeronautics and Astronautics, Nanjing 210016, China
[3] AVIC (Aviation Industry Corporation of China) (Chengdu) Unmanned Aerial Vehicle System Co., Ltd., Chengdu 611743, China
[4] College of Aerospace Engineering, Nanjing University of Aeronautics and Astronautics, Nanjing 210016, China
* Correspondence: zhenlongwu@nuaa.edu.cn

Abstract

This investigation designs grilles of two configurations inside an S-shaped inlet for UAVs. The present work numerically investigates the effects of the configurations, numbers, diameters, and lengths of the grilles on the inlet aerodynamic performance under different flight conditions, such as airflow Mach number, angle of attack, and sideslip angle. The influences of the baseline configuration, Configuration 1, and Configuration 2 on the aerodynamic performance of the inlet are systematically compared. The numerical results show that after installing the grilles, the total pressure recovery decreases by an average of 5.42% for Configuration 1 and 3.46% for Configuration 2. In terms of the absolute circumferential total pressure distortion, which decreases by 1.26% for Configuration 1 and 2.34% for Configuration 2, the swirl distortion index of Configuration 2 approaches zero. It is found that a large sideslip angle significantly degrades the inlet performance, and Configuration 1 experiences the maximum decline of approximately 0.0124 in the total pressure recovery. Based on the optimized design of Configuration 1, the optimal parameters are determined as 5 grille rows, a grille diameter of 4 mm, and a grille length of 6 mm. This configuration achieves an optimal balance between flow regulation and resistance suppression, with a maximum total pressure recovery of 0.9884 and the absolute circumferential total pressure distortion controlled below 0.015. This study clarifies the optimization direction of key parameters for grilles and provides a theoretical basis and technical reference for the design of UAV S-shaped inlet and grille integrations.

Keywords: UAV; S-shaped inlet; grille; aerodynamic performance

Check for updates

Academic Editor: Bosko Rasuo

Received: 31 December 2025
Revised: 24 January 2026
Accepted: 27 January 2026
Published: 29 January 2026

Copyright: © 2026 by the authors. Licensee MDPI, Basel, Switzerland. This article is an open access article distributed under the terms and conditions of the Creative Commons Attribution (CC BY) license.

1. Introduction

Unmanned aerial vehicles (UAVs) play a vital role in both civilian and military sectors and are widely deployed in critical missions such as persistent surveillance, communication relay, and emergency logistics, thus demonstrating exceptional strategic and practical value [1]. Representative examples include the MQ-series Predator UAVs of the United States, as well as the Pterodactyl and CH series UAVs developed in China. As a key aerodynamic component of the engine, the aerodynamic performance of the inlet is directly related to the operating efficiency of the engine and the overall performance of the aircraft.

To meet the requirements of UAVs, such as stealth performance and aerodynamic performance, researchers have proposed the S-duct inlet. However, its insufficient aerodynamic performance is attributed to the complex internal flow mechanism and swirl characteristics inside the duct, which are mainly reflected by two indices, namely the total pressure recovery coefficient and outlet flow distortion [2]. In terms of flow characteristics of subsonic S-bend inlets, scholars all over the world have conducted fruitful investigations [3–5]. Ming et al. [6] combined large eddy simulation (LES) with various flow field decomposition techniques, revealing that under high Reynolds number conditions, the dual-vortex flow pattern dominates the annular region near the wall of the S-duct inlet, and downstream turbulent mixing effectively suppresses the development of flow distortion and swirl. Wang et al. [7] analyzed the effects of key geometric parameters on the performance of S-duct inlets via numerical simulation and evaluated the total pressure recovery coefficient and total pressure distortion index at the outlet of S-duct inlets using a backpropagation (BP) neural network. The average prediction error was approximately 3.9% compared with the numerical simulation results. Sadatpour et al. [8] combined a genetic algorithm with an artificial neural network to optimize the aerodynamic performance of S-duct inlets, achieving a reduction in total pressure loss and flow distortion.

During actual flight, UAVs are exposed to a variety of complex meteorological conditions. As the "respiratory tract" of the propulsion system, the inlet generates intense negative pressure, which causes hailstones and ice crystals in the air to be sucked into the engine interior. This in turn triggers engine surge, flameout, power loss, and other malfunctions, posing a severe threat to flight safety [9,10]. Scholars have conducted in-depth exploration and research on the adverse effects of in-flight icing on fixed-wing UAVs [11,12] and rotary-wing UAVs [13,14]. Therefore, the inlet anti-icing/de-icing technology is a key technology for ensuring the stable flow of air inside the inlet during aircraft flight. Common types of inlet anti-icing/de-icing technologies include chemical de-icing, mechanical de-icing, and thermal anti-icing [15,16]. The mechanical de-icing system first breaks the ice into fragments via mechanical means and then removes the crushed ice particles through the action of airflow scouring, centrifugal force, or vibration effects. However, due to the inherent limitations of UAVs, such as limited payload capacity and low available power, the anti-icing/de-icing technologies that have been maturely applied on manned aircraft may not be directly adaptable to UAVs [17,18]. To address this issue, a grille is introduced at the front end of the inlet outlet.

Most research on grille technology applications has focused on engine integration, stealth technology, and electromagnetic interference (EMI) shielding. Rumpf et al. [19] clarified the technical advantages of grilles, which can be directly applied to the integrated design of diffusers and combustors in advanced aeroengines. They experimentally verified that this technology can achieve excellent flow-straightening effects. Chiccine et al. [20] positioned the grille at the combustor inlet for the RJ43-MA-3 ramjet engine. The research results demonstrated that this technology can effectively reduce the level of flow distortion at the combustor inlet, thereby providing support for the stable operation of the engine. Piercy et al. [21] conducted experiments by incorporating a grille into the inlet system of a hypersonic engine. The results showed that this approach can effectively reduce flow distortion, but at the expense of the total pressure recovery coefficient. In addition, research has been conducted on the stealth performance and radar wave shielding effectiveness of grilles, which has enabled the realization of stealth capabilities and EMI shielding functions [22,23].

It can be seen from the above research that most studies either focus solely on inlets or concentrate on grilles—specifically, the flow straightening effects of grilles in engines, as well as grille-related stealth technology and EMI shielding research. By contrast, there have

been few reports on the internal flow characteristics of the integrated UAV/inlet/grille configuration. In this paper, based on an integrated UAV/S-shaped inlet/grille configuration, the effects of different grille configurations on the internal flow field structure and aerodynamic performance of the inlet are investigated via numerical simulation methods. The second chapter describes the numerical method, including the numerical model, numerical setup, grid independence study, and methodical validation. The third chapter defines the performance parameters involved in the text. The four chapters analyze the influence of laws of inlet aerodynamic performance and flow field structure from the perspectives of freestream Mach number, angle of attack, sideslip angle, and configuration optimization, respectively.

2. Numerical Method

2.1. Geometric Model

Figure 1 shows the integrated geometric model of the UAV, the inlet, and the grille, with specific parameters listed in Table 1. A grille is designed at the rear section of the inlet, forming two schemes (Configuration 1: cross-shaped grille; Configuration 2: I-shaped grille). Figure 1 illustrates the model parametric definitions of the different grille configurations, whose top section is composed of a rectangle and two identical semicircles.

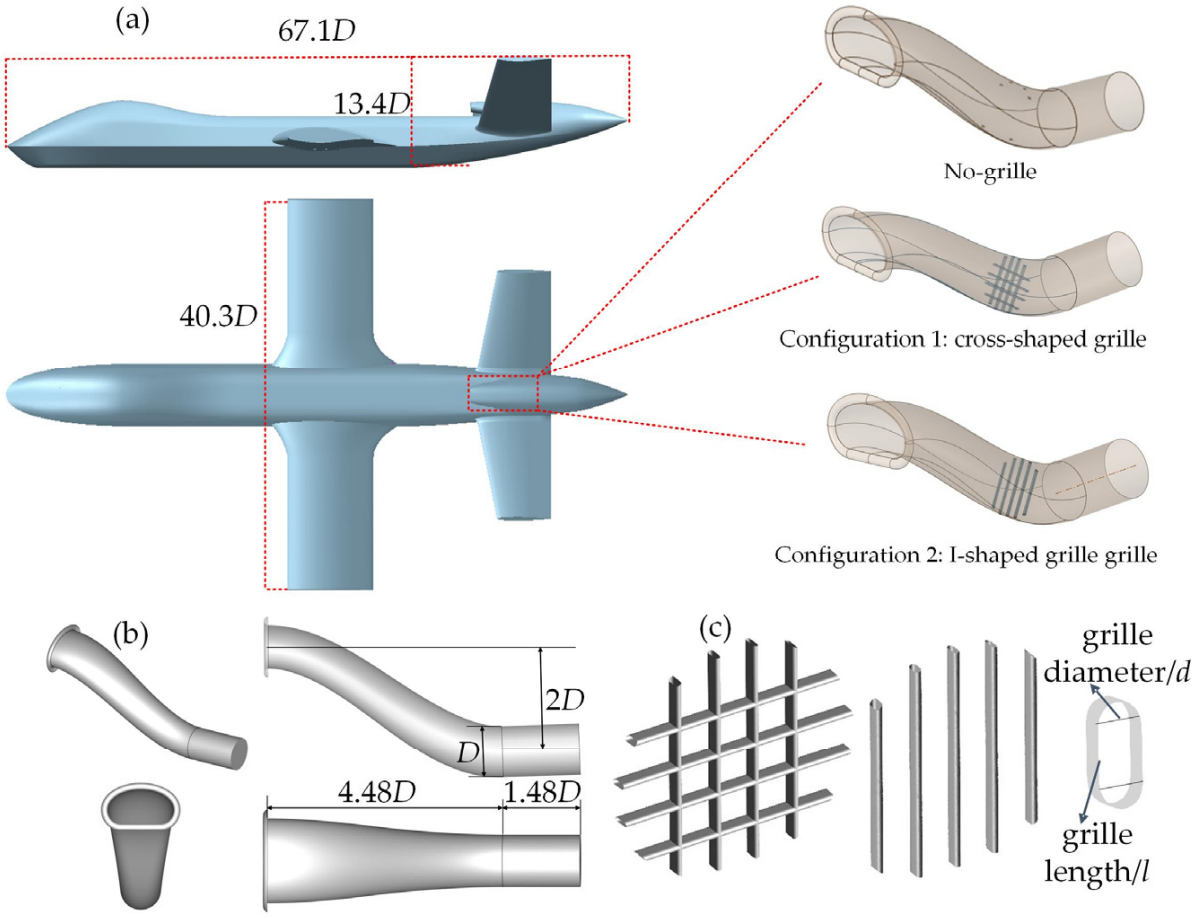

Figure 1. The integrated geometric model of the UAV, the inlet, and the grille: (**a**) aircraft, (**b**) inlet, (**c**) grille.

Table 1. Geometric parameters of the S-shaped inlet.

Parameter	Value
Diameter of AIP	*D*
Total length of the inlet	4.48 *D*
Centerline offset of the inlet	2 *D*
Length of the constant-area straight section	1.48 *D*
Total length of the aircraft	67.1 *D*
Total width of the aircraft	40.3 *D*
Total height of the aircraft	13.4 *D*

2.2. Numerical Setup and Mesh

Figure 2 shows the computational domain and mesh used in the present simulations. The length of the computational domain is 805 *D*, as well as the width of 403 *D*, and the height of 268 *D*. The boundary conditions for the numerical simulation were set according to Figure 2. The boundary surfaces at the downstream of the computational domain and the outlet of the model are set as pressure outlets. The remaining boundaries of the computational domain are all set as pressure far-fields. The surfaces of the aircraft body, inlet, and grille were set to non-slip adiabatic wall boundary conditions, which simulate the no-slip effect of the air near the wall and ensure that there is no heat transfer between the fluid and the solid surfaces. These boundary conditions are considered appropriate for the numerical simulation and were used consistently across different inlet models.

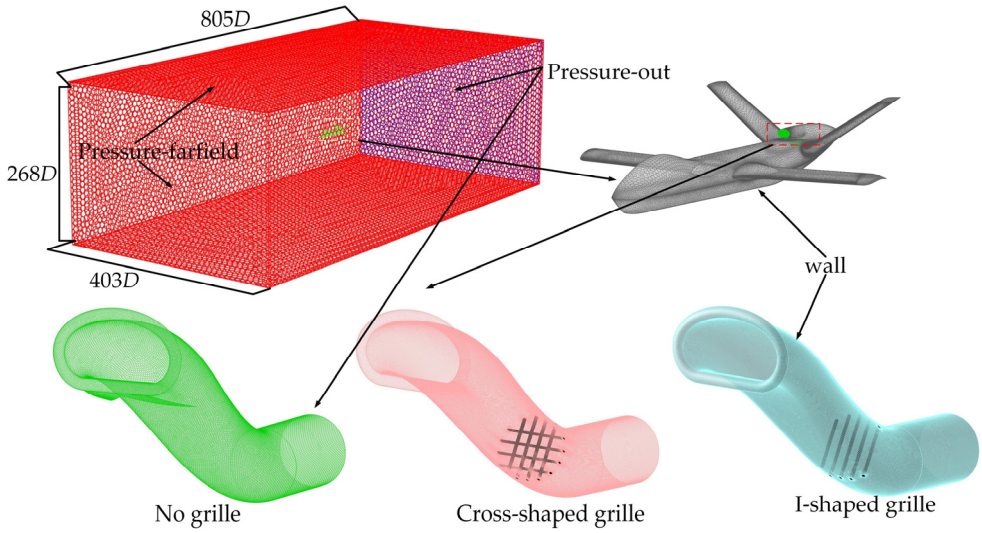

Figure 2. Mesh of the 3D numerical model of the different inlet configurations.

The Fluent Meshing 2021 R1 software is adopted for mesh generation of the flow domain, and the mesh is a hybrid unstructured mesh consisting of triangular and polygonal elements. Figure 3 shows the computational domain mesh and model mesh used in the present simulations. Necessary mesh refinement is implemented in regions with large flow parameter gradients, such as near the wall and inside the inlet. The boundary layer mesh is properly adjusted to maintain the accuracy of the simulation. The final number of boundary layers is set to 20, with the first layer of mesh height being 0.05 mm and a growth rate of 1.2. In this paper, we only focus on the flow field characteristics inside the inlet and the aerodynamic performance of the inlet. Therefore, the grid resolution for the inlet has been

ensured to be fine to guarantee that all the y+ values on the walls of the inlet and grille are well below 1, complying with the near-wall resolution requirement for the k-ω SST model. However, to save the computational cost and to keep a high computational efficiency, the grids of the fuselage and wing can be coarser, more or less, since these components do not influence the inlet. This grid setting leads to some values of y+ on the walls of the fuselage and wings above 1.

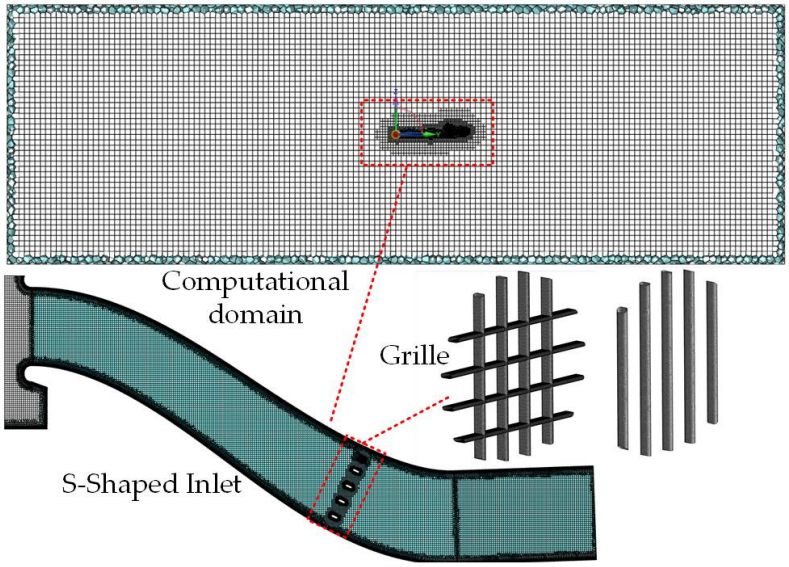

Figure 3. Computational mesh.

This study employs the commercial software Ansys Fluent 2021 R1 to perform numerical computations for the detailed flow field characteristics inside the UAV/inlet/grille system, and the finite volume method is adopted to discretize the three-dimensional Reynolds-averaged Navier–Stokes (RANS) equations based on density correction. The fluid is assumed to be an ideal gas with constant specific heat (γ = 1.4), and the variation in molecular viscosity coefficient follows the Sutherland formula. During the solution process, the point implicit (Gauss–Seidel) method is used for time marching to accelerate convergence, the Roe scheme is used to discretize the viscous convective fluxes, and the left and right state values at the interface are obtained through second-order accurate interpolation. The flow equations and turbulence model equations are discretized using the second-order upwind scheme and the first-order upwind scheme. The RANS equations of continuity and momentum are expressed in Equations (1) and (2), and the modeled energy equation is expressed in Equation (3).

$$\frac{\partial}{\partial x_i}(\rho u_i) = 0 \tag{1}$$

$$\frac{\partial}{\partial x_j}(\rho u_i u_j) = -\frac{\partial p}{\partial x_i} + \frac{\partial \tau_{ij}}{\partial x_j} + \frac{\partial}{\partial x_j}\left(-\rho\overline{u_i' u_j'}\right) \tag{2}$$

$$\frac{\partial}{\partial x_i}[u_i(\rho E + p)] = \frac{\partial}{\partial x_j}\left(k\frac{\partial T}{\partial x_j}\right) + \frac{\partial}{\partial x_j}(\tau_{ij} u_i) \tag{3}$$

where $\tau_{ij} = \mu\left(\frac{\partial u_i}{\partial x_j} + \frac{\partial u_j}{\partial x_i}\right) - \frac{2}{3}\mu\frac{\partial u_k}{\partial x_k}\delta_{ij}$, u_i is the air velocity vector, as well as the position vector x_i, p is pressure, μ is air molecular dynamic viscosity, T is temperature, δ_{ij} is the Kronecker delta function, k is the thermal conductivity, and E is the total energy. The term $\rho\overline{u_i' u_j'}$ corresponds to the Reynolds stress, which is modeled using the $k-\omega$ shear-

stress transport (SST) turbulence model to provide closure for Equation (2). The turbulent viscosity is computed by $k-\omega$ SST closure, which enables efficient near-wall turbulence resolution with reliable performance in free-shear flow conditions [24]. This model has been widely applied to the study of the internal flow of air inlets [25,26]. It has become one of the most widely utilized turbulence models in the aerospace field.

2.3. Performance Parameter Definition

The main aerodynamic performance indices used to evaluate and quantify the subsonic UAV inlet are the total pressure recovery coefficient(σ), circumferential total pressure distortion index ($\Delta\sigma_0$), and swirl angle(θ) at the AIP (Aerodynamic Interface Plane), which are defined as follows:

(1) Total pressure recovery coefficient is defined as follows:

$$\sigma = {P_{AIP}}^* / {P_0}^* \tag{4}$$

where ${P_0}^*$ is the freestream total pressure, ${P_{AIP}}^*$ is the area-weighted average of the total pressure at the AIP of the inlet.

(2) Circumferential total pressure distortion index is defined as follows:

$$\Delta\sigma_0 = \left(P^*_{60,min} - P^*_{AIP}\right) / P^*_{AIP} \tag{5}$$

where $P^*_{60,\min}$ is the minimum value of the average total pressure over the 60° sector obtained via circumferential scanning on the AIP, and it is evident that the value is negative.

(3) The swirl angle(θ) is proposed to evaluate the swirl intensity, which is defined as follows [27]:

$$\theta = arctan\left(V_0 / V_y\right) \tag{6}$$

where as illustrated in Figure 4, V_0 denotes the tangential velocity at the AIP, and V_y denotes the axial velocity at the AIP. Furthermore, the swirl distortion index($R_{\theta,abs7}$) is defined as the area ratio of the region where the absolute value of the swirl angle at the AIP exceeds 7°.

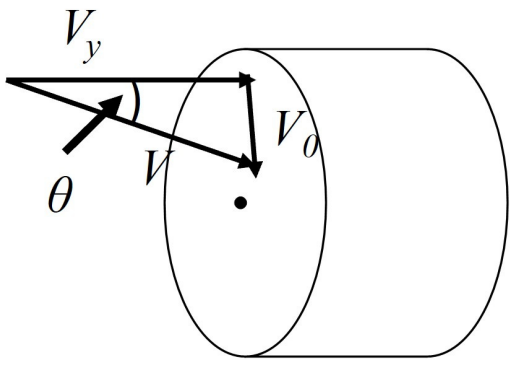

Figure 4. Schematic definition of swirl angle.

2.4. Mesh Independence Study

To confirm that the present numerical simulation is independent of the mesh configuration, for Configuration 1 (the cross-shaped grille), three sets of meshes with 5 million, 10 million, and 15 million cells were generated and adapted to calculate at the same settings and conditions. The comparison of the total pressure recovery and vorticity at the AIP for different meshes is depicted in Figure 5.

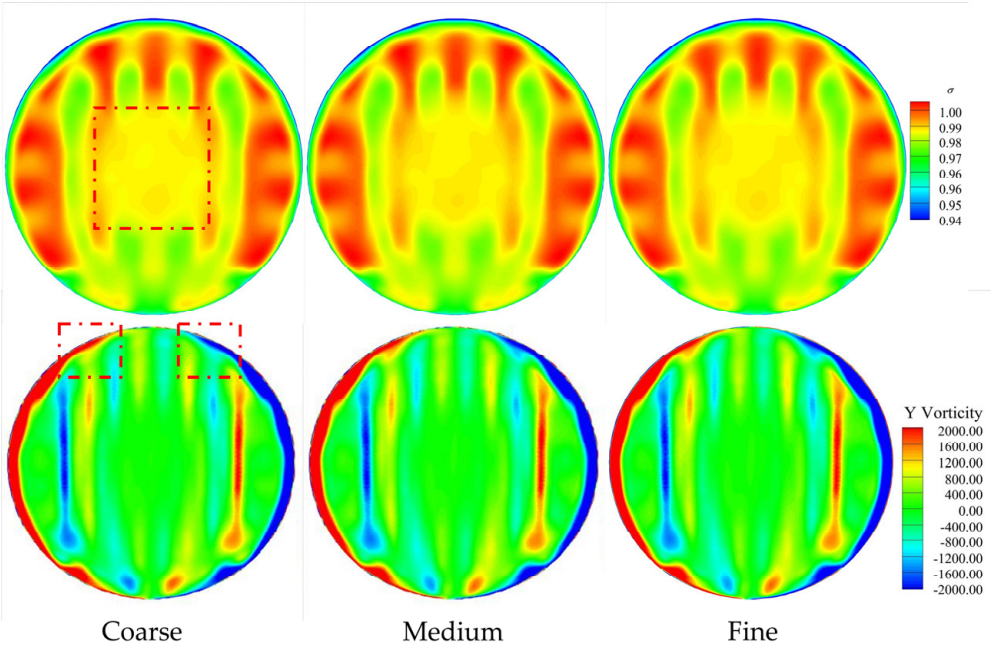

Figure 5. Comparison of the total pressure and vorticity contours at the AIP calculated with different levels of mesh resolutions.

From the contour maps, the calculated results of the medium and fine meshes are in good agreement. The results of coarse mesh for total pressure distribution in the central region of the AIP and for vorticity distribution in the top region of the AIP exhibit certain discrepancies compared with those from medium and fine meshes. Furthermore, Table 2 quantitatively compares the aerodynamic performance parameters at the AIP for three different meshes. The results indicate that the total pressure recovery coefficients of the medium mesh and fine mesh are close, while that of the coarse mesh is reduced by approximately 0.0013 compared with the other two grids. The circumferential total pressure distortion results of the three grid systems are similar.

Table 2. Comparison of aerodynamic performance parameters at the AIP with different levels of mesh resolutions.

Run	*H*/km	*MFR*/(kg/s)	M_0	*Total Pressure*/Pa	*Total Temperature*/K	α/°	β/°	σ	$\Delta\sigma_0$
Coarse	7	1.97	0.1	41,393.59	243.19	0	0	0.9846	−0.0041
Medium								0.9858	−0.0046
Fine								0.9860	−0.0049

In addition, Figure 6 presents the static pressure distributions on the top and bottom surfaces of the UAV inlet. In Figure 5, the coordinates are normalized; the abscissa is the ratio of the wall coordinate x to the distance L from the intake to the AIP section, and P_0 denotes the freestream static pressure in the far field. It can be observed that the calculation results of the coarse mesh are slightly different from those of the other two meshes, while the results of the medium and fine meshes are basically consistent. In summary, it can be concluded that the results of the medium mesh have basically achieved convergence. Considering both computational efficiency and computational accuracy, the subsequent calculations are performed with the medium mesh as the reference. In summary, the total mesh count of the baseline configuration is determined to be approximately 6 million, that of the I-shaped grille configuration around 6.5 million, and that of the cross-shaped grille

configuration roughly 10 million, which fully captures the aerodynamic profiles of the aircraft/inlet/grille integration.

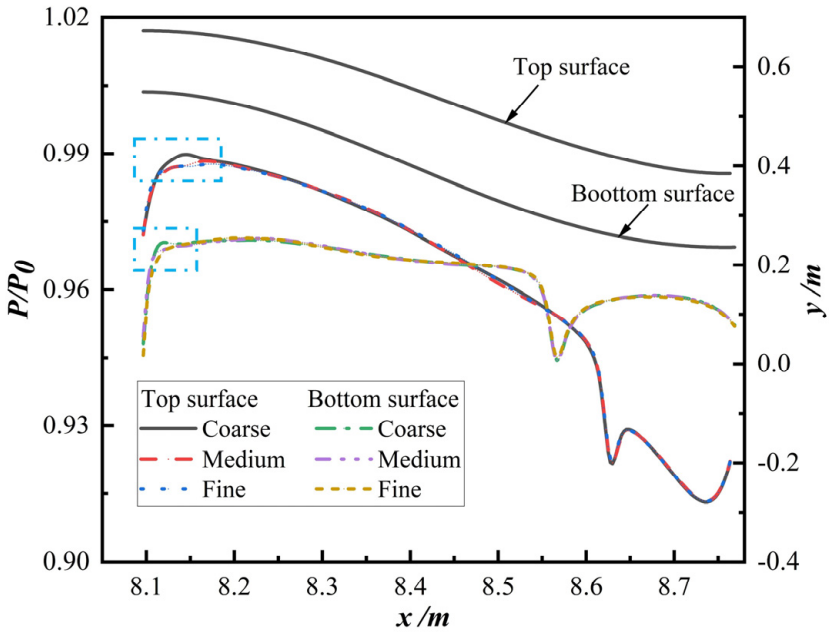

Figure 6. Static pressure distributions on the top and bottom surfaces under different mesh levels.

2.5. Methodological Validation

To verify the credibility of the numerical method adopted in this paper. Under the conditions of M_0 = 0.2, H = 7 km, TP (Total Pressure) = 42,267.63 Pa, TT (Total Temperature) = 244.64 K, α = 0° and β = 0°, three operating points were randomly calculated for the inlet outlet backpressure of different configurations. The calculation results are represented by the green lines in Figure 7. The intersection points of these results with the three inlet-engine flow matching lines were taken as validation points to inversely calculate the total pressure recovery coefficient. The calculation results are presented in Table 3, with the maximum deviation from the theoretical values of each matching line being no more than 0.003.

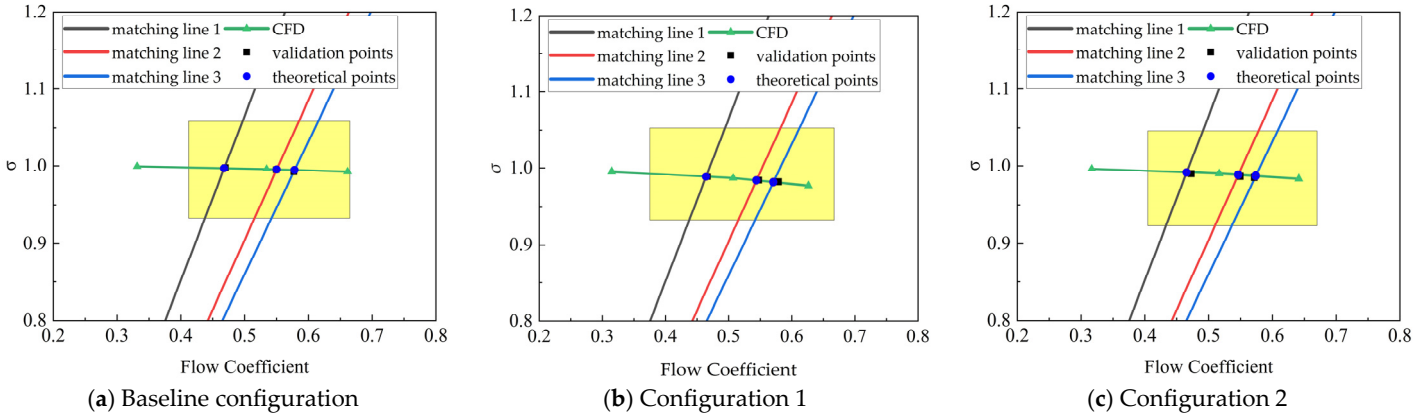

(**a**) Baseline configuration (**b**) Configuration 1 (**c**) Configuration 2

Figure 7. Comparison between simulation validation points and theoretical points for different inlet configurations.

Table 3. Calculation results of case validation for different inlet configurations.

Configuration	Theoretical Value		Numerical Value	
	Flow Coefficient	σ	Flow Coefficient	σ
Baseline configuration	0.468	0.9969	0.470	0.9976
	0.550	0.9953	0.550	0.9949
	0.578	0.9946	0.577	0.9925
Configuration 1	0.464	0.9888	0.466	0.9888
	0.544	0.9839	0.548	0.9841
	0.571	0.9817	0.580	0.9821
Configuration 2	0.465	0.9916	0.473	0.9900
	0.546	0.9885	0.550	0.9865
	0.574	0.9871	0.572	0.9852

In addition, Ren et al. [28] conducted a wind tunnel experimental study on the aerodynamic characteristics of a deflected double 90° S-duct inlet/volute for unmanned aerial vehicles. Under the same operating conditions with freestream airspeed V_0 = 90 m/s, TP = 106,373.61 Pa, TT = 288.15 K, $\alpha = 0°$, $\beta = 0°$, MFR (mass flow rate) = 4.4 kg/s, numerical simulations of the UAV were performed using the numerical method proposed in this paper, and a comparison between the simulation results and experimental data is presented in Figure 8. Although there are minor discrepancies between the numerical simulation results and experimental data, the overall trends are consistent.

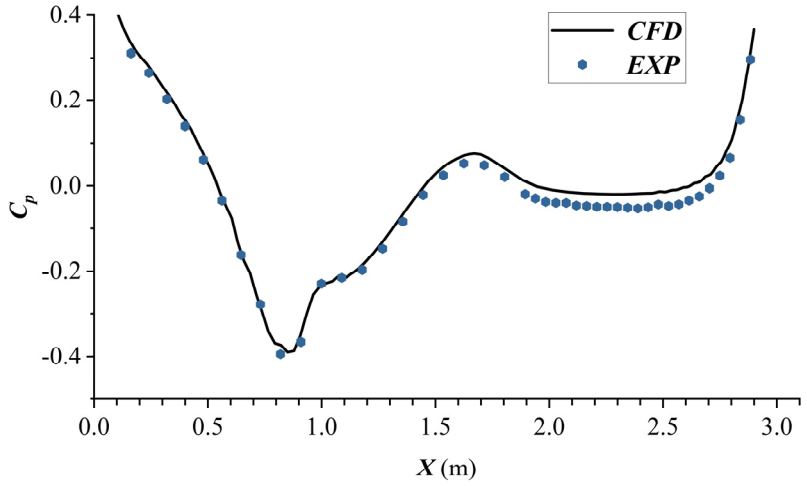

Figure 8. Comparison of experimental [28] and numerical results for surface static pressure.

3. Results and Discussion

3.1. Effect of Freestream Mach Number

With a constant mass flow rate at the inlet and outlet, the computational conditions for investigating the variation trend of the aerodynamic performance of the air inlet with the freestream Mach number at an altitude of 7 km are listed in Table 4, and the specific results are shown in Figure 9.

Table 4. Flight conditions under different freestream Mach numbers.

	H/km	*MFR*/(kg/s)	M_0	*Total Pressure*/Pa	*Total Temperature*/K	*α*/°	*β*/°
Computational condition	7	2.32	0.1	41,393.59	243.19	0	0
			0.2	42,267.63	244.64		
			0.3	43,753.55	247.07		

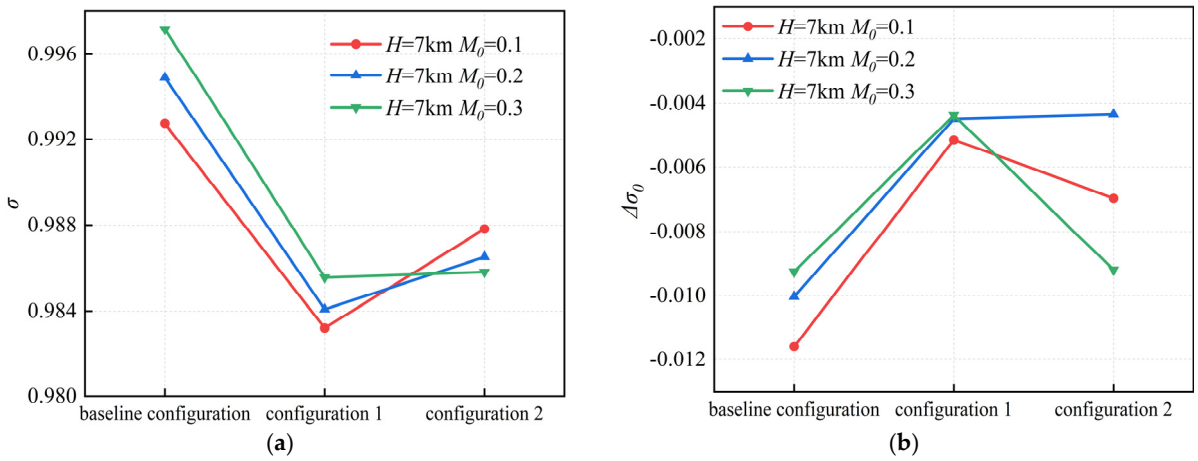

Figure 9. Aerodynamic performance of distinct configurations under different freestream Mach numbers. (**a**) the total pressure recovery coefficient, (**b**) the circumferential total pressure distortion index.

It can be seen from the simulation results that under the high-altitude condition, with the increase in the freestream Mach number, the ram compression effect of the inlet is enhanced. The total pressure recovery coefficient of the baseline configuration (without a grille) and Configuration 1 is improved, while that of Configuration 2 shows the opposite trend. The total pressure recovery coefficients of the three configurations remain above 0.9800 under all working conditions, indicating that the inlet has excellent aerodynamic performance. It is also observed that the total pressure recovery coefficient decreases after the installation of grilles. Among them, Configuration 1 suffers a larger total pressure loss due to its larger blocking area. The absolute circumferential total pressure distortion values are all below 0.012, which verifies the superior circumferential total pressure distortion performance of the inlet. On the whole, the grilles contribute to the improvement of the circumferential total pressure distortion index of the inlet, but the improvement effect varies with configurations. With the increase in the freestream velocity, the total pressure distortion of Configuration 1 changes slightly, while that of Configuration 2 shows a significant difference. This phenomenon demonstrates that Configuration 1 has a stronger adaptability at this altitude, and its flow field is less affected by the freestream Mach number.

Figure 10 illustrates the aerodynamic performance of streamwise cross-sections of various inlet configurations under different freestream Mach numbers. For the baseline configuration, at low airflow velocities, the pressure distributions at the two bends are opposite due to the effect of centrifugal force, which results in a large low-pressure zone in the lower-middle region of the AIP surface. As the flow velocity increases, the kinetic energy of the airflow entering the inlet rises. Meanwhile, the centrifugal force acting on the airflow passing through the two bends intensifies. This enhanced kinetic energy can suppress the initiation and development of flow separation, leading to the concentration of the low-pressure zone at the bottom of the AIP surface. After the installation of grilles, the

total pressure distribution on the AIP surface varies with the grille configuration, which also increases the flow complexity at the outlet cross-section. Although the grilles can suppress flow separation and vortices to a certain extent and improve flow stability, the resistance introduced by the grilles will cause an increase in total pressure loss. Consequently, the flow permeability of the configured inlets decreases, and the area of the low-pressure zone expands. It can also be observed that with the increase in freestream Mach number, the uniformity of the total pressure distribution on the AIP surface of Configuration 1 changes slightly, while that of Configuration 2 first improves and then deteriorates.

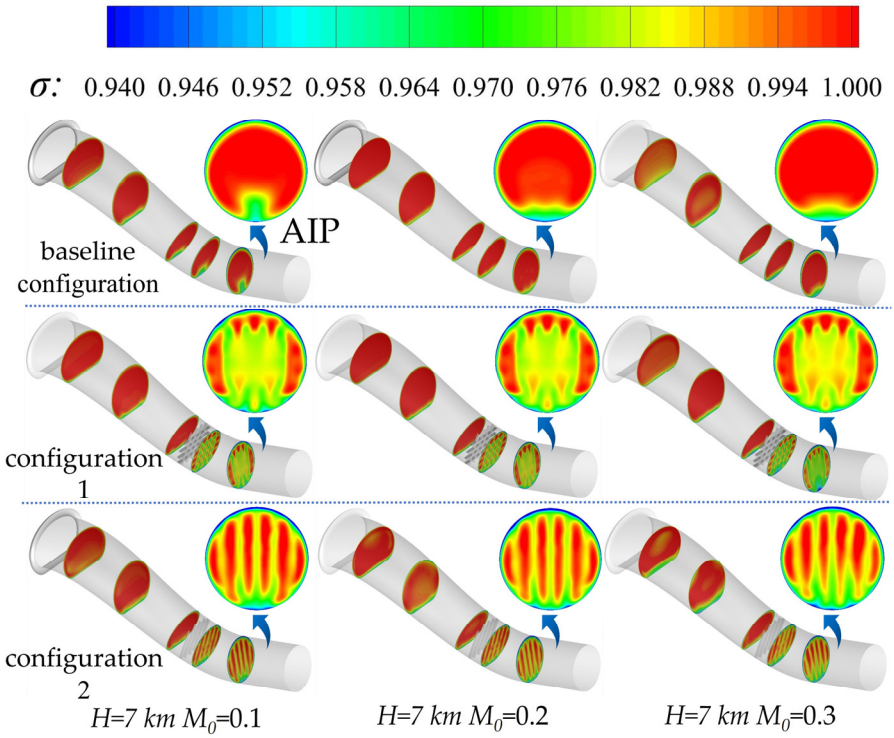

Figure 10. Contour of total pressure recovery coefficient for streamwise cross-sections of various inlet configurations under different freestream Mach numbers.

Figure 11 presents the contour of Mach number, secondary streamlines, and vorticity at the AIP section for various inlet configurations under different freestream Mach numbers. Under the low-speed freestream condition of the baseline configuration, the pressure distributions at the two bends are opposite, and the transverse adverse pressure gradient induces secondary vortices with opposite directions. Consequently, counter-rotating vortices are generated at the inlet and outlet, forming symmetric vorticity clusters. Combined with the total pressure distribution, this leads to local low total pressure regions. As the ram effect intensifies, the flow separation at the bottom of the AIP is suppressed, and the airflow develops along the wall surface, forming separation and vorticity regions on both sides of the wall. With the integration of the grille, the flow structure evolves from the counter-rotating vortex pattern: for Configuration 1, the bottom vortex structure transforms into symmetric small-scale vortices, accompanied by alternating positive and negative vorticity strips, indicating the generation of periodic vortex pairs in the flow field. For Configuration 2, the flow evolves into disordered small-scale vortices with more distorted secondary streamlines. However, the separation vortices on both sides of the wall are attenuated, and the contrast and width of the vorticity strips are further increased, which suggests that the intensity and scale of the vortex structures are significantly enhanced, and the flow field becomes more complex.

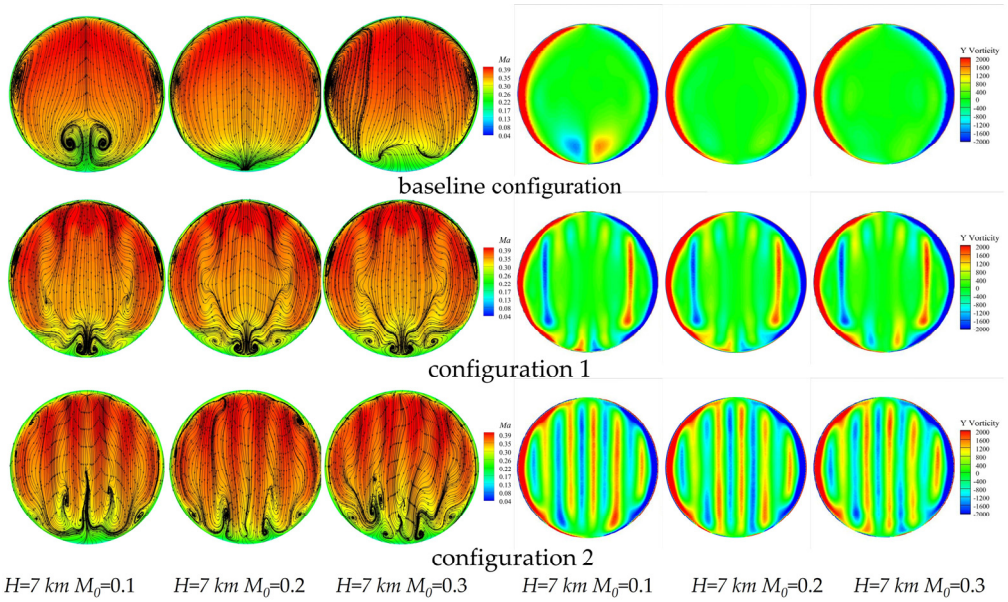

Figure 11. Contours of Mach number, secondary streamlines, and vorticity at the AIP section for various inlet configurations under different freestream Mach numbers.

Figure 12 presents the contour of Mach number and secondary streamlines on the symmetry planes of various inlet configurations under different freestream Mach numbers. It can be observed that for the baseline configuration at low flow velocities, the streamlines at the second bend deflect upward as a whole. As the airflow energy increases, it can better overcome the effects induced by transverse airflow, and the streamlines transit more smoothly along the flow direction. The installation of grilles mitigates the vortex and turbulence phenomena in the flow field, thereby optimizing the swirling flow state. Consequently, the flow field achieves a more stable velocity distribution.

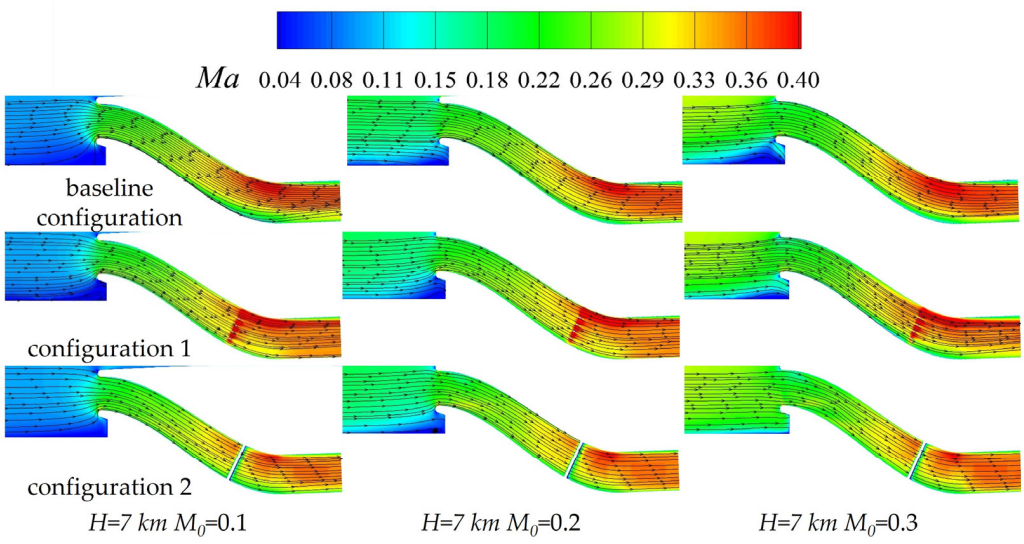

Figure 12. Contour of Mach number and secondary streamlines on the symmetry planes of various inlet configurations under different freestream Mach numbers.

Figure 13 illustrates the swirl flow characteristics of the various inlet configurations at different freestream Mach numbers. With the variation in configurations, the swirling flow distortion index decreases under all freestream conditions. Combined with the results in Figure 10, it is indicated that the grilles exert a certain improvement effect on the swirling flow characteristics inside the inlet and possess a favorable flow rectification capability. It

can also be seen that Configuration 2 achieves a more significant improvement in vortex characteristics and exhibits superior swirling flow performance.

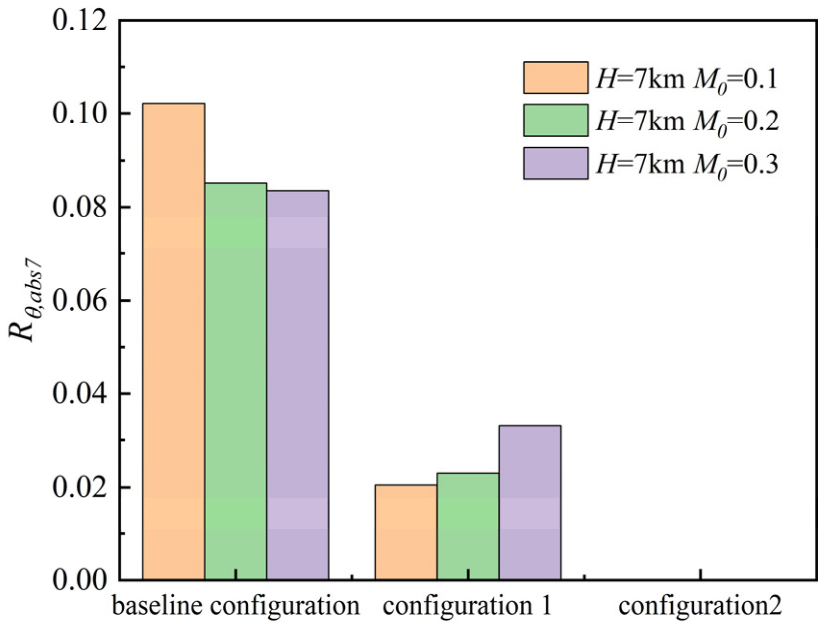

Figure 13. Swirl flow characteristics of the various inlet configurations at different freestream Mach numbers.

3.2. Effect of Angle of Attack and Sideslip Angle

Angle of attack and sideslip angle are the primary parameters for determining the flight attitude of UAVs. With the outlet mass flow rate kept constant, the effects of different combined angles on the aerodynamic performance of various inlet configurations were investigated at an altitude of 7 km, and the results are listed in Table 5, and the calculation results are presented in Figure 14. It can be observed that, except for the case M_0 = 0.2, α = 12°, and β = 16°, the total pressure recovery coefficient exhibits a variation trend of decreasing and then increasing with the change in configurations. Moreover, the total pressure loss is relatively large under the conditions of α = 12° and β = 16°. Configuration 1 yields the minimum absolute value of the circumferential total pressure distortion index under large angles of attack, while Configuration 2 under sideslip angles. Furthermore, all configurations exhibit poorer aerodynamic performance under the condition of large sideslip angles.

Table 5. Flight conditions under different combined angles.

	***H*/km**	***MFR*/(kg/s)**	M_0	***Total Pressure*/Pa**	***Total Temperature*/K**	**α/°**	**β/°**
Computational condition	7	2.32	0.1	41,393.59	243.19	12	16
			0.2	42,267.63	244.64	−6	16
						0	16
						−6	0
						12	16
						12	0

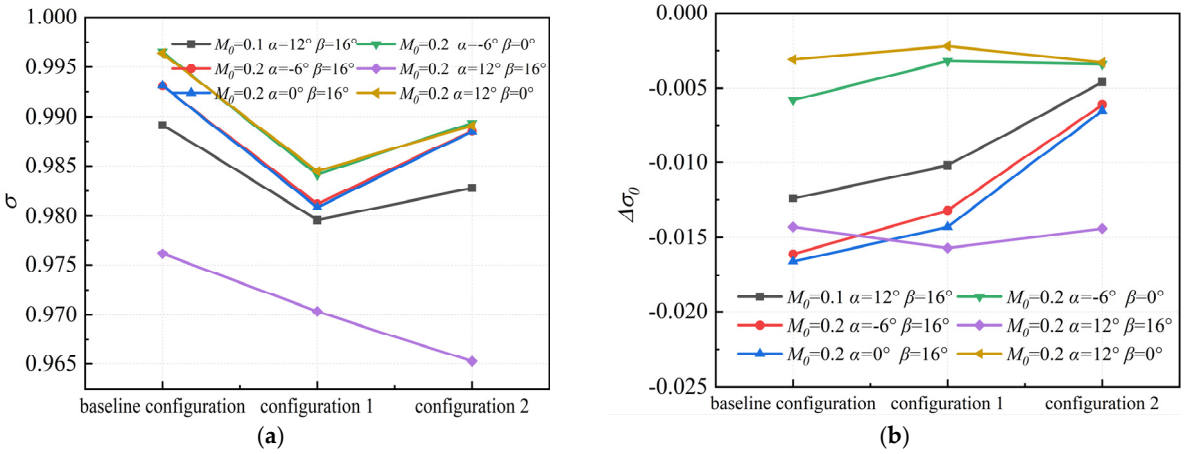

Figure 14. Aerodynamic performance of distinct configurations under combined angle conditions. (**a**) the total pressure recovery coefficient, (**b**) the circumferential total pressure distortion index.

Figure 15 presents the contour of the total pressure recovery coefficient for streamwise cross-sections of various inlet configurations under large angles of attack and sideslip. For the baseline configuration, the presence of a large sideslip angle induces flow separation on the left side of the lower wall surface, generating distinct large-scale vortices. A large-area low-pressure zone forms around the vortex cores. After the installation of grilles, the airflow is forced to distribute and flow along the passage, which effectively alleviates the degree of flow separation. Configuration 2 achieves a more significant improvement effect, with a more uniform total pressure distribution. The condition of large angles of attack exerts a minor influence on the flow field structures of the three configurations. This further indicates that the aerodynamic performance of the inlet is more sensitive to the sideslip angle. Under the conditions of large angles of attack and large sideslip angles, a relatively large separation zone persists in the lower-left region along the streamwise direction of the inlets for all three configurations. Moreover, after the installation of grilles, the area of the low-pressure zone expands, and the airflow becomes more turbulent. At this point, the resistance introduced by the grilles outweighs the benefits, resulting in the degradation of the inlet aerodynamic performance. This phenomenon arises from the mismatch between the inlet and the grille caused by the forced flow rectification design of the two components. Therefore, in accordance with the relevant design criteria, the inlet and the grille should be collaboratively designed as an integrated system to achieve mutual compatibility.

It appears from Figure 16 that the presence of a large sideslip angle induces a large-scale separation vortex on the left side of the AIP for both the baseline configuration and Configuration 1. In contrast, Configuration 2 achieves a superior flow rectification effect, breaking down the separation vortex into several small-scale separation vortices with improved vorticity periodicity. Under the condition of a high angle of attack, the separation vortices of the baseline configuration are located on both sides of the wall. With the integration of grids, the separation vortices on both sides of the wall are attenuated, while small-scale counter-rotating vortices are generated at the bottom. Under the coupling of sideslip angle and angle of attack, both configurations develop a large-scale single-vortex structure and form a vorticity cluster dominated by negative vorticity. The distribution of positive and negative vorticity regions becomes diffused with deteriorated symmetry, indicating a state of intense flow shear. These results demonstrate that the sideslip angle has a more significant impact on the aerodynamic performance of the inlet than the angle of attack.

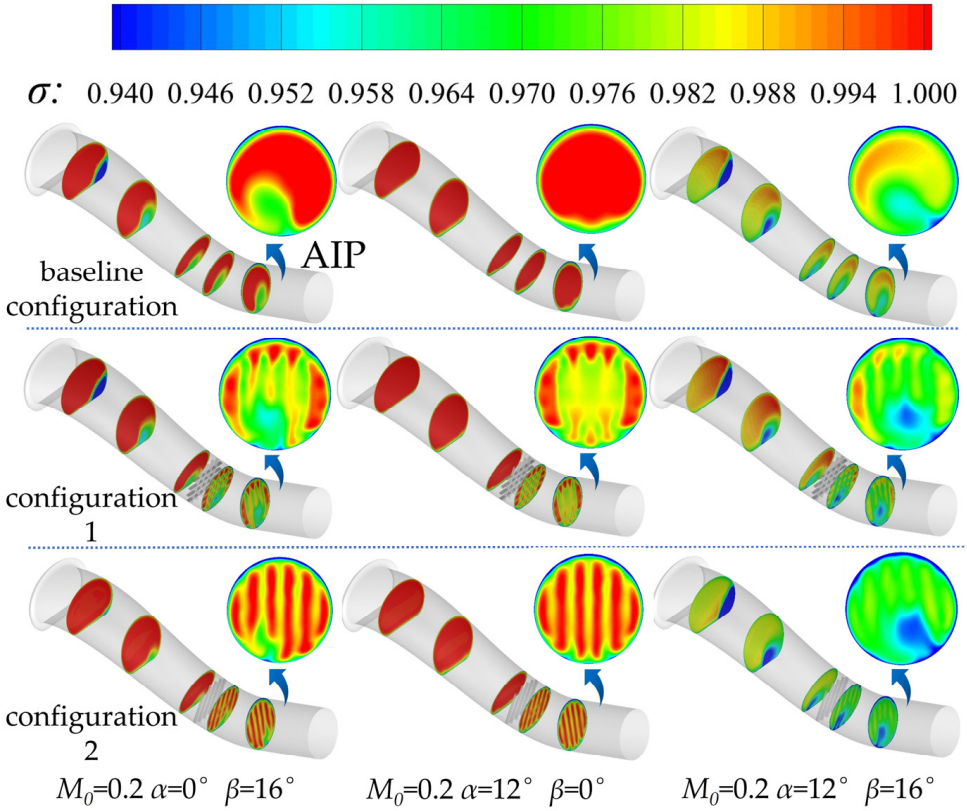

Figure 15. Contour of total pressure recovery coefficient for streamwise cross-sections of various inlet configurations under large angles of attack and sideslip.

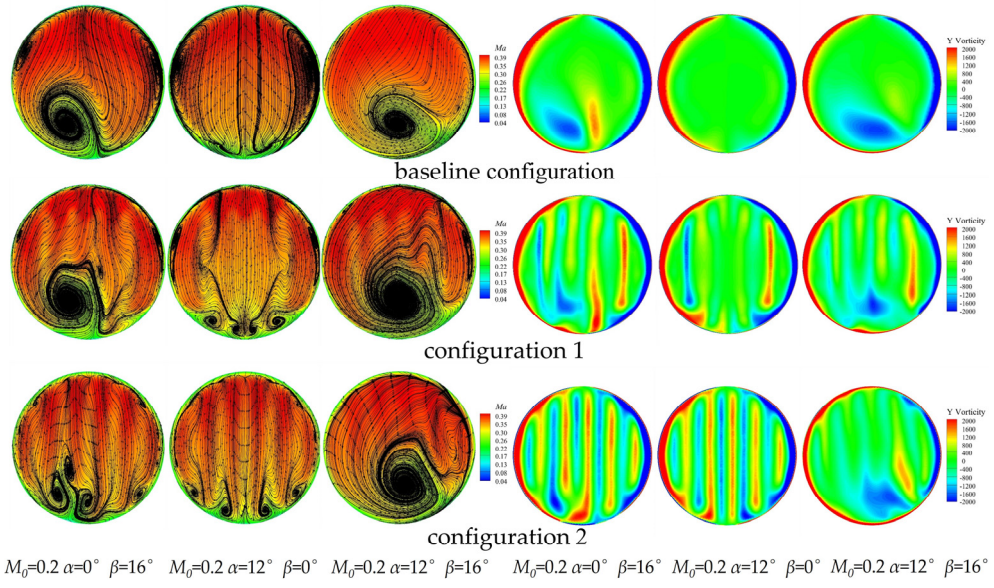

Figure 16. Contours of Mach number, secondary streamlines and vorticity at the AIP section for various inlet configurations under large angles of attack and sideslip.

It can be observed from Figure 17 that the installation of grilles significantly increases the airflow deflection degree at the inlet under large sideslip angles, which induces flow separation in the lip region and thus leads to intense transverse airflow. The flow rectification effect of Configuration 1 is significantly inferior to that of Configuration 2; the flow field of Configuration 2 develops steadily along the axial direction, with the velocity field transiting smoothly along the streamwise direction and no significant disturbance or transverse airflow occurring. However, under the combined extreme angles, the internal

flow fields of the inlets with the three configurations exhibit significant turbulence, resulting in an increase in the energy loss of the inlets.

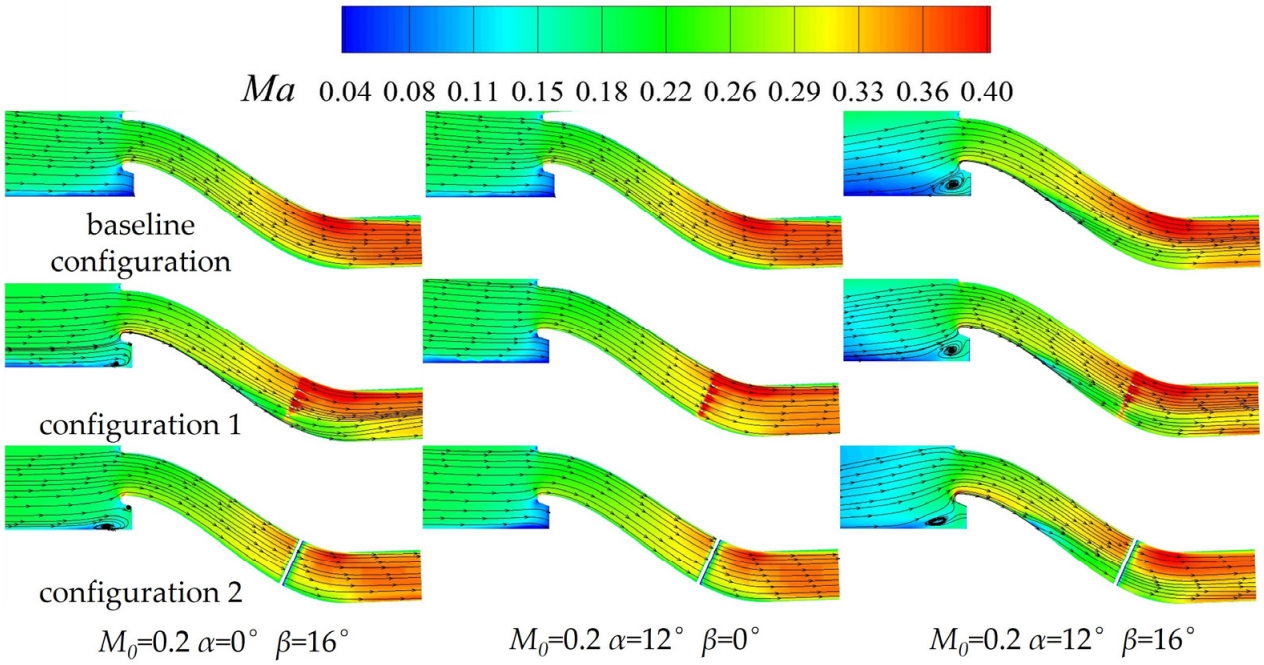

Figure 17. Contour of Mach number and secondary streamlines on the symmetry planes of various inlet configurations under large angles of attack and sideslip.

It can be observed from Figure 17 that the installation of grilles significantly increases the airflow deflection degree at the inlet under large sideslip angles. As illustrated in the figure, the incorporation of the grille leads to a significant increase in the airflow deflection degree at the inlet duct entrance under a large sideslip angle. The incoming flow direction is no longer parallel to the symmetry plane of the inlet lip, accompanied by a sharp rise in the lateral velocity component of the lip surface. This phenomenon intensifies the adverse pressure gradient, triggering strong lateral airflow movement and inducing flow separation in the inlet region. Upon entering the inlet, the flow field of Configuration 2 develops steadily along the axial direction, with a smooth transition of the velocity field along the flow path and no significant disturbances or lateral flow. In contrast, the flow straightening performance of Configuration 1 is notably inferior to that of Configuration 2. Under the combined extreme angle condition, the sideslip angle has already resulted in flow asymmetry between the left and right lips, which is further exacerbated by the angle of attack. Due to the strong adverse pressure gradient, the low-energy airflow fails to maintain wall-attached flow, eventually forming a distinct separation zone at the lip. Additionally, the internal flow fields of the inlets with the three configurations exhibit significant turbulence, which contributes to an increase in the energy loss of the inlet duct.

As shown in Figure 18, under different combined angles, the swirling flow distortion index decreases with the variation in configurations. For all three configurations, the operating conditions corresponding to the larger swirling flow distortion index are all under large sideslip angles, which further explains that the aerodynamic performance of the inlet is more sensitive to the sideslip angle.

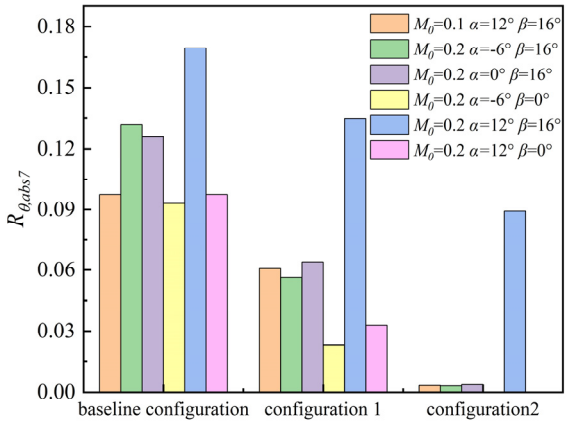

Figure 18. Swirl flow characteristics of the various inlet configurations at combined angle conditions.

Overall, a comparative analysis of the aerodynamic performance of different inlet configurations under various operating conditions reveals that Configuration 1 exhibits the most significant reduction in total pressure recovery coefficient, while Configuration 2 performs marginally better than Configuration 1, though both are inferior to the baseline configuration. Moreover, the grilles consistently exert a flow rectification effect and effectively improve flow uniformity. Given that extreme aerodynamic attitudes are rarely encountered in actual UAV flight conditions, the present study demonstrates that the I-shaped grille configuration achieves optimal compatibility with the inlet. Subsequent research will therefore focus on the optimal design based on Configuration 2.

3.3. Optimization Design of Grille Number

The number of grilles exerts an influence by modulating the grille open area ratio: a greater number of grilles induces stronger airflow obstruction and more intense flow disturbance. To investigate the effect of grille quantity on the aerodynamic performance of the inlet under typical operating conditions, as shown in Table 6. The discussion concerning grille diameter and length employs identical operating conditions.

Table 6. Flight conditions for different grille numbers under various combined operating conditions.

	***H*/km**	***M*$_0$**	***Total Pressure*/Pa**	***Total Temperature*/K**	**α/°**	**β/°**
Computational condition	0	0	101,325	288.15	0	0
	7	0.1	41,393.59	243.19	0	0
		0.2	42,267.63	244.64	0	0
					0	16
					12	16
		0.3	43,753.55	247.07	0	0

The calculation results are presented in Figure 19. With the exception of the operating condition corresponding to M_0 = 0.2, α = 12°, and β = 16°, the total pressure recovery coefficient increases initially and then decreases with the increasing number of grilles across all other conditions, with the maximum total pressure loss occurring when the grille number reaches 6. Meanwhile, the absolute value of the circumferential total pressure distortion index follows the same trend of first decreasing and then increasing, which indicates that the flow rectification effect of the grilles improves initially but deteriorates subsequently as the number of grilles increases.

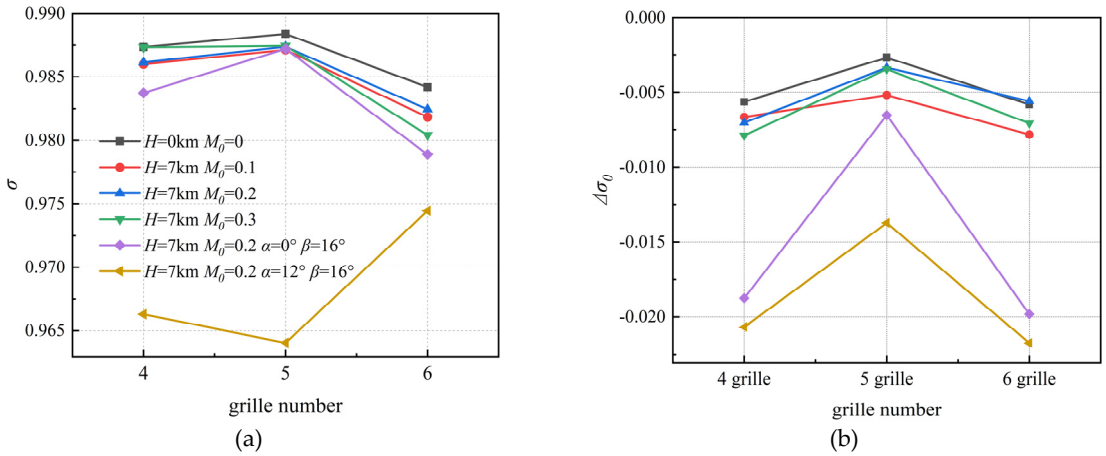

Figure 19. Aerodynamic performance of different grille numbers under various operating conditions. (**a**) the total pressure recovery coefficient, (**b**) the circumferential total pressure distortion index.

Figure 20 presents the contour plots of the total pressure recovery coefficient for streamwise cross-sections of inlets with different grille numbers under combined operating conditions. In the absence of aerodynamic attitudes, the 4 grille rows configuration features a relatively wide flow passage, resulting in insufficient flow rectification performance; consequently, symmetric separation vortices form at the bottom of the AIP plane, accompanied by an extensive low-pressure zone. Although the 6 grille rows configuration can suppress flow separation, it suffers from reduced multi-channel open area ratio and increased flow resistance, which in turn renders the flow field more turbulent. The 5 grille rows configuration achieves an optimal balance between separation vortex control and flow resistance mitigation, characterized by smaller-scale separation vortices and a more uniform pressure distribution. As the sideslip angle increases to 16°, the symmetry of the flow field is disrupted. Owing to its more refined flow division and control, the 5 grille rows configuration exhibits superior flow stability, with a separation zone significantly smaller than those of the 4 grille rows and 6 grille rows configurations. Under compound-angle conditions, the combined effects of freestream congestion at the upper lip induced by the angle of attack and intense transverse flow driven by the yaw angle give rise to large-scale, unsteady separation vortex structures. Although the 6 grille rows configuration effectively improves the inlet flow field structure and reduces the area of the low-pressure zone via flow rectification, the increase in grille number leads to higher structural mass and greater structural complexity. Therefore, there exists an optimal range of grille numbers during the inlet/grille design process, which requires a trade-off between aerodynamic performance gains and structural complexity/weight.

It can be observed from Figure 21 that under a freestream with a large sideslip angle alone, the flow field structure changes significantly. Specifically, the separation region on the lower inner wall of the inlet is exacerbated, and a large-scale, unsteady separation vortex structure forms in the second bend of the S-duct. After rectification by the 5 grille rows configuration, the airflow is split from a large-scale single vortex structure into multiple small-scale vortices, with a more periodic vorticity distribution. At the 6 grille rows configuration, the vortex structure intensity peaks, accompanied by larger positive/negative vorticity regions and poorer uniformity. This indicates enhanced flow dissipation, further demonstrating that the 5 grille rows configuration achieves an optimal balance between separation vortex control and flow resistance.

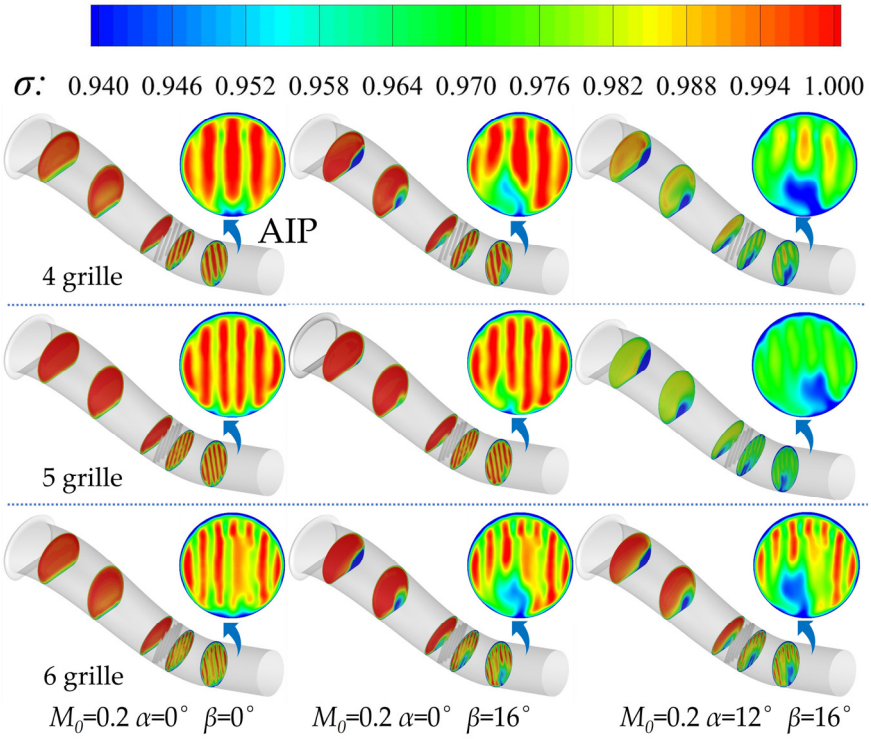

Figure 20. Contour of total pressure recovery coefficient for streamwise cross-sections of inlets with different grille numbers under combined operating conditions.

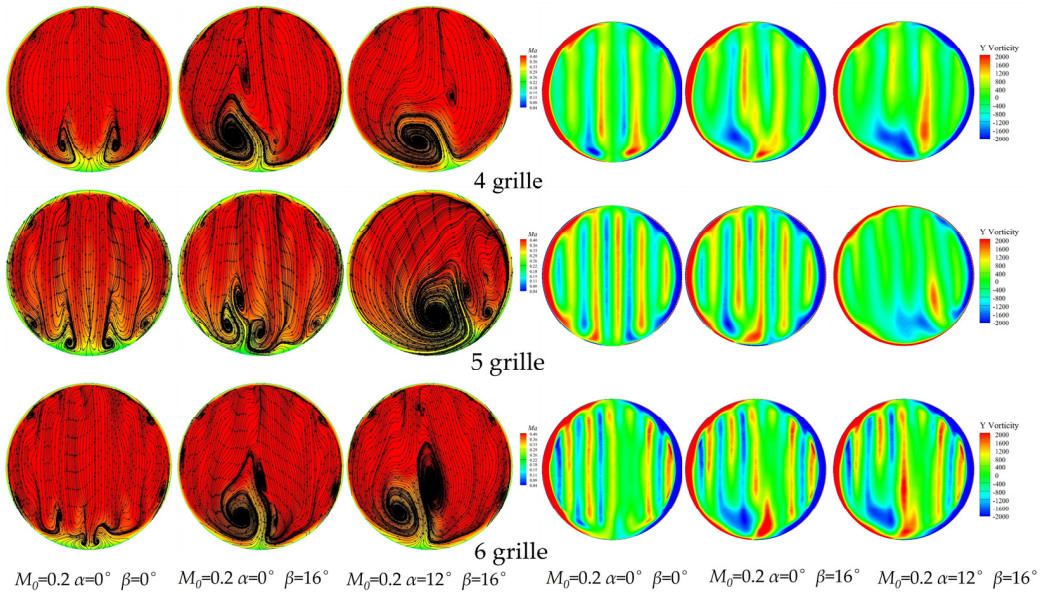

Figure 21. Contours of Mach number, secondary streamlines, and vorticity at the AIP section of different grille numbers under combined operating conditions.

It can be observed from Figure 22 that an excessive number of grilles leads to over-constraint on the airflow and a consequent increase in flow resistance, whereas an insufficient number of grilles results in inadequate constraint and poor flow rectification performance. Neither of these two configurations can effectively suppress the transverse development of the airflow, with localized low-Mach-number regions emerging at the curved sections in both cases. In contrast, the 5 grille rows configuration achieves a more uniform flow velocity distribution, with the airflow inside the inlet discharging more closely to a straight, axial direction. Furthermore, the flow field distortion becomes most severe under low-angle conditions, where the low-Mach-number regions expand and degrade the

outlet flow field quality. Furthermore, when the airflow is parallel and has not yet entered the inlet, airflow impinges on the wall surface, leading to a reduction in airflow kinetic energy and the formation of a low-velocity zone at the lower end of the lip, while no flow separation occurs. With the introduction of a sideslip angle, the 5 grille rows configuration effectively improves the internal velocity distribution of the inlet duct. However, for the 4 and 6 grille row configurations, the influence of the low-velocity zone in the second bend extends to the lip, resulting in a relatively high airflow velocity at this location, which reduces the adverse pressure gradient and prevents flow separation at the lower end of the lip. Under the combined angle condition, although low-velocity zones are observed inside the inlets of all three configurations, the 6-grille-row configuration is notably more affected by the introduction of the angle of attack. A strong adverse pressure gradient is induced at the lip, leading to significant flow separation that adversely affects the incoming flow.

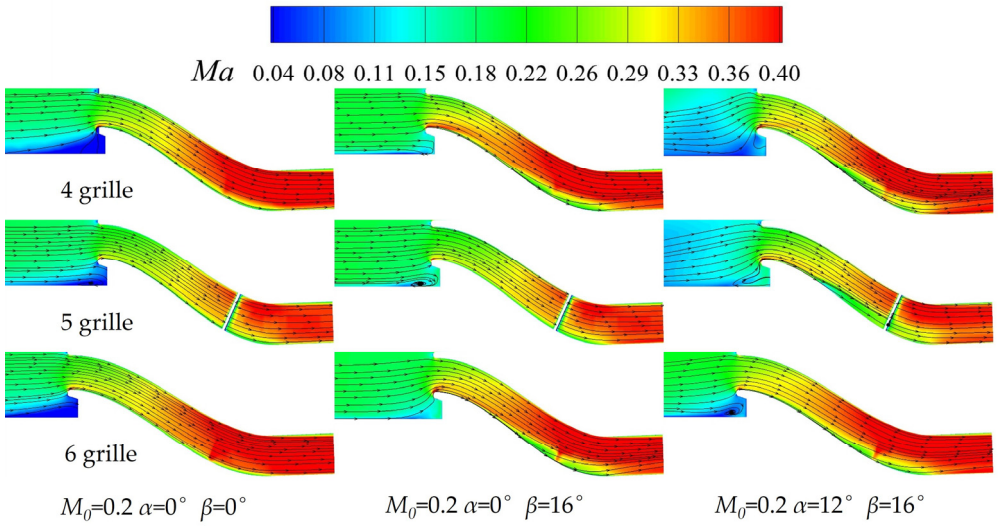

Figure 22. Contour of Mach number and secondary streamlines on the symmetry planes of different grille numbers under combined operating conditions.

In summary, extreme aerodynamic attitudes rarely occur during UAV flight. Additionally, based on the comparison of aerodynamic performance parameters of inlet configurations with different grille numbers. The 5 grille rows configuration is deemed suitable and thus selected as the object for subsequent optimization.

3.4. Optimization Design of Grille Diameter

In this study, the grilles adopt a smooth semicircular structure at both the leading and trailing ends, with a cylindrical structure in the middle section. Taking the 5 grille rows configuration as the baseline, the influence of grille diameter on the aerodynamic performance of the inlet was investigated, and the calculation results are presented in Figure 23. With the exception of the operating condition corresponding to M_0 = 0.2, α = 12°, and β = 16°, the variation trends of the total pressure recovery coefficient and the absolute value of the circumferential total pressure distortion index are consistent with those observed when the number of grilles was varied. Notably, at a grille diameter of 3 mm, the total pressure recovery remains at a relatively high level under this specific operating condition.

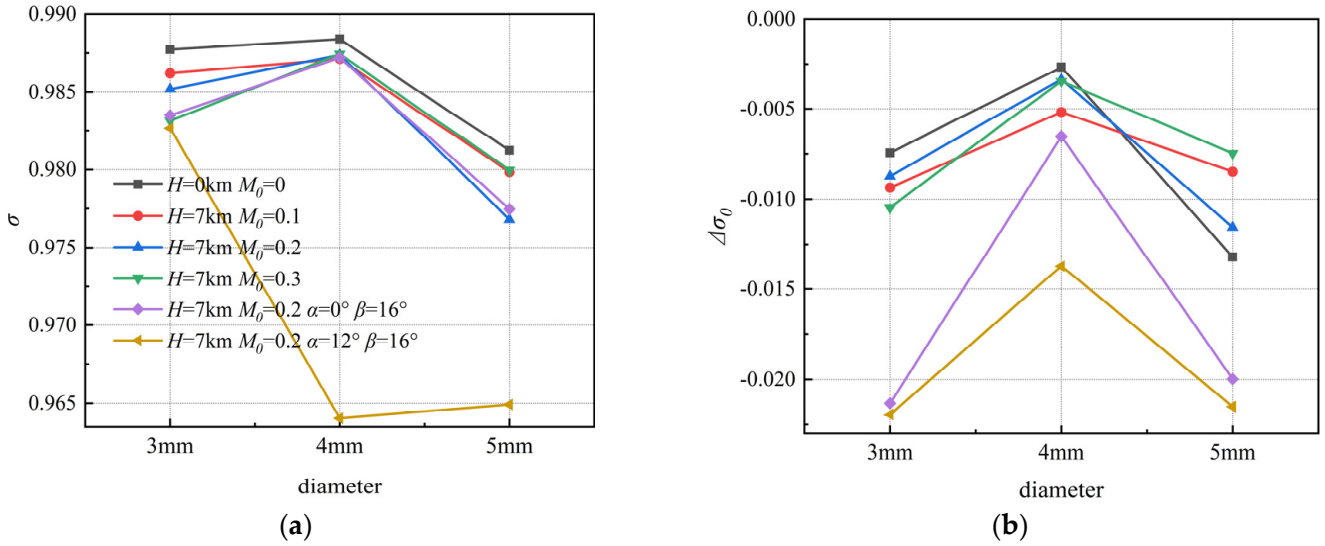

Figure 23. Aerodynamic performance of different grille diameters under various operating conditions. (**a**) he total pressure recovery coefficient, (**b**) The circumferential total pressure distortion index.

It can be observed from Figure 24 that under the condition of no aerodynamic attitude, the AIP plane exhibits comparable pressure distributions for both relatively large and small grille diameters. However, at a grille diameter of 5 mm, total pressure loss is more pronounced, and the low-pressure zone extends over a larger area. The regulatory effect of grille diameter on inlet performance becomes far more critical under asymmetric freestream conditions. When the sideslip angle is 16°, the configuration with d = 4 mm imparts a more optimal flow-around curvature to the incoming flow, effectively mitigating streamwise flow separation within the inlet and drastically reducing the extent of the low-pressure zone on the AIP plane. With the introduction of a large angle of attack, the inlet flow field structure undergoes negligible variation at d =3 mm, which corroborates that the total pressure recovery coefficient remains at a relatively high level. In contrast, larger grille diameters induce the formation of large-scale separation vortices in the upstream region; these vortices propagate downstream and consequently give rise to extensive low-total-pressure zones and severe flow distortion. Although altering the grille diameter also indirectly modulates the grille open area ratio, its impact on the inlet flow field differs from that induced by varying the number of grilles.

It can be noted from Figure 25 that when the d =3 mm, and there is no aerodynamic attitude, the overall streamlines are symmetrically and parallelly distributed, with only slight curling at the AIP bottom. This indicates that the flow is in a weak shear state, where only localized flow separation occurs, and no large-scale vortices are formed. The vorticity field is entirely in a low-amplitude state. Under the action of asymmetric incoming flow, large-scale vortices emerge at the bottom, and the spatial scale of vorticity strips expands further, which reflects the increase in asymmetric disturbances. As the grille diameter increases to 4 mm, the vorticity field presents a clear periodic strip structure of positive-negative vortex pairs. When the grille diameter continues to increase, the frictional loss induced by the grille exceeds the flow field gain, and the vorticity-concentrated regions reappear with an increased amplitude, indicating that the vortex scale becomes larger again.

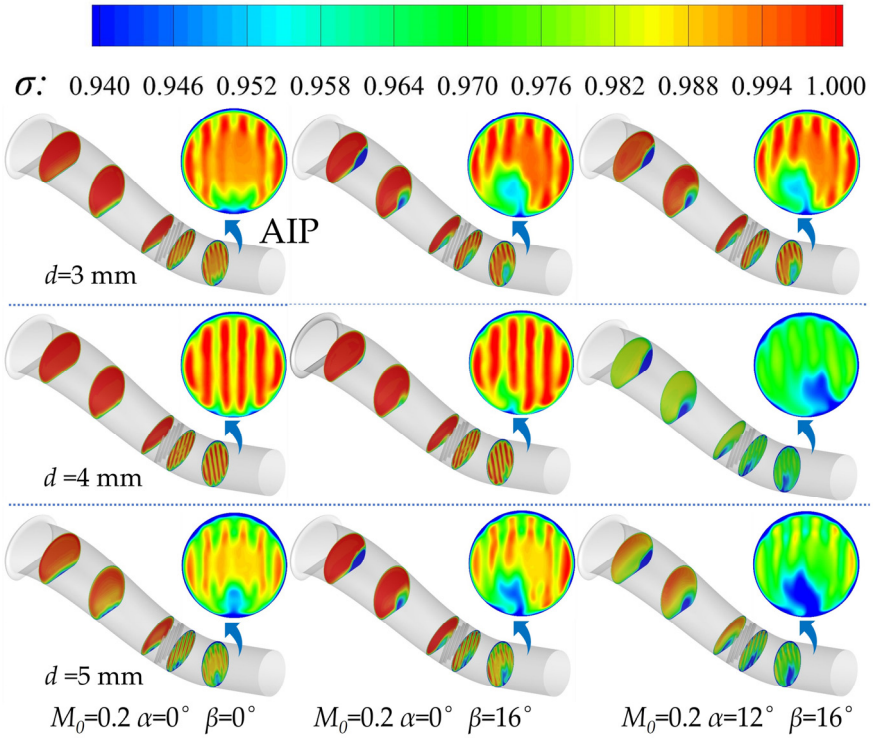

Figure 24. Contour of total pressure recovery coefficient for streamwise cross-sections of inlets with different grille diameters under combined operating conditions.

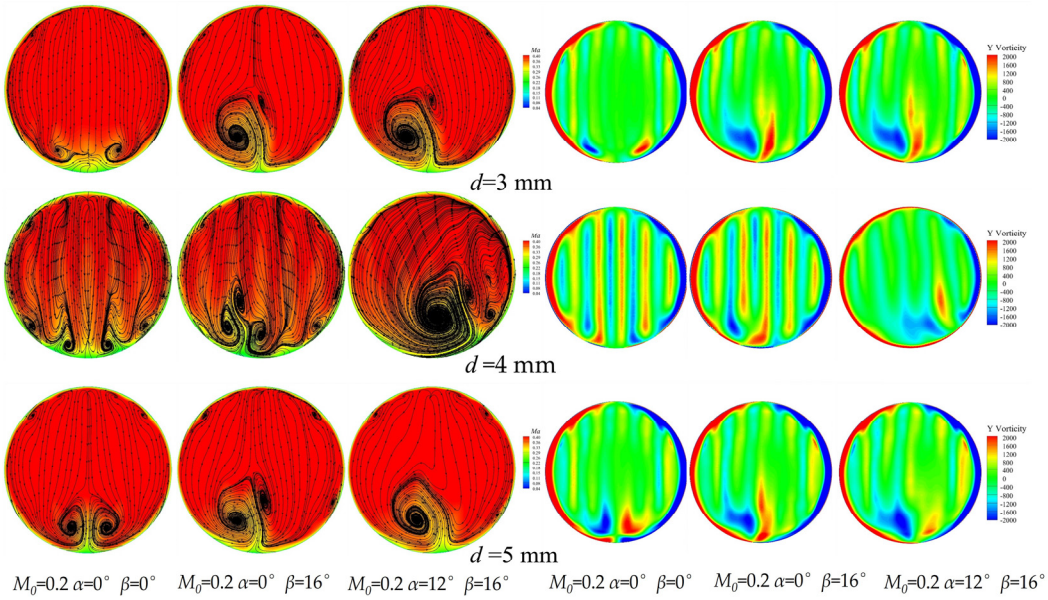

Figure 25. Contours of Mach number, secondary streamlines, and vorticity at the AIP section of different grille diameters under combined operating conditions.

It can be observed from Figure 26 that the regulating effect of the grille with a diameter of 3 mm is limited. In contrast, when the diameter is increased to 4 mm, the flow field structure on the symmetry plane undergoes a distinct transformation. Specifically, the low-velocity zone on the lower wall inside the inlet is suppressed and elongated, yielding a more uniform velocity distribution. Consequently, the quality of the outlet airflow is significantly enhanced, achieving the design objective of maximizing the regulating effect while minimizing the blocking effect. With a further increase in grille diameter, the blocking effect of the grille on the airflow is intensified, and the low-velocity zone re-

emerges. Evidently, the flow field stability of the configuration with d = 4 mm is markedly superior to that of the other two configurations. Furthermore, at a large sideslip angle, a distinct separation zone is formed at the lower lip, primarily attributed to the asymmetry of the incoming flow. With the introduction of the angle of attack, adjusting the grille diameter results in the manifestation of the grille's flow regulation effect, which reduces the adverse pressure gradient and facilitates the airflow in overcoming this gradient.

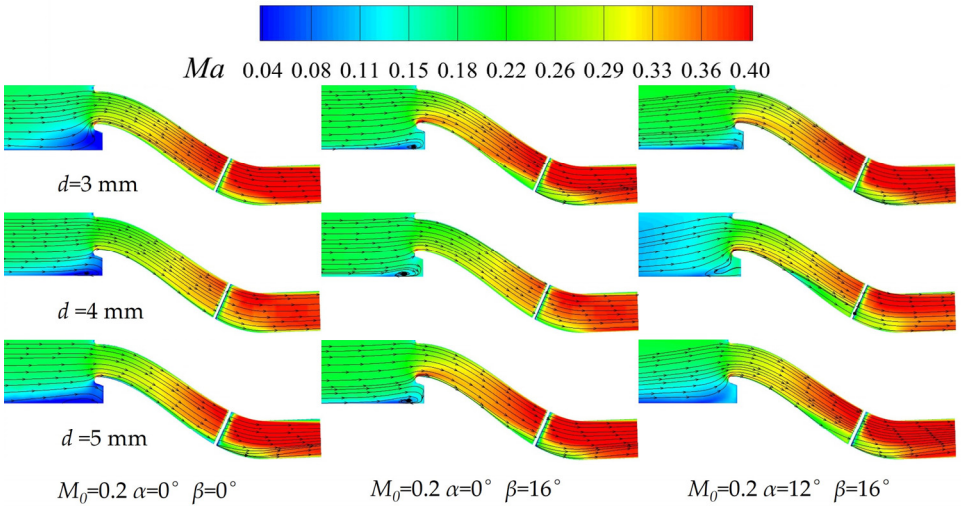

Figure 26. Contour of Mach number and secondary streamlines on the symmetry planes of different grille diameters under combined operating conditions.

Similarly, the grille configuration with a diameter of 4 mm is deemed suitable and thus selected as the object for subsequent optimization.

3.5. Optimization Design of Grille Length

Grille length is defined as the length of the cylindrical structure of the grille. Based on the optimal grille number and diameter, the influence of grille length on the aerodynamic performance of the inlet was investigated, and a preferable grille design was ultimately derived. The calculation results are presented in Figure 27, and their variation trends are consistent with those discussed above.

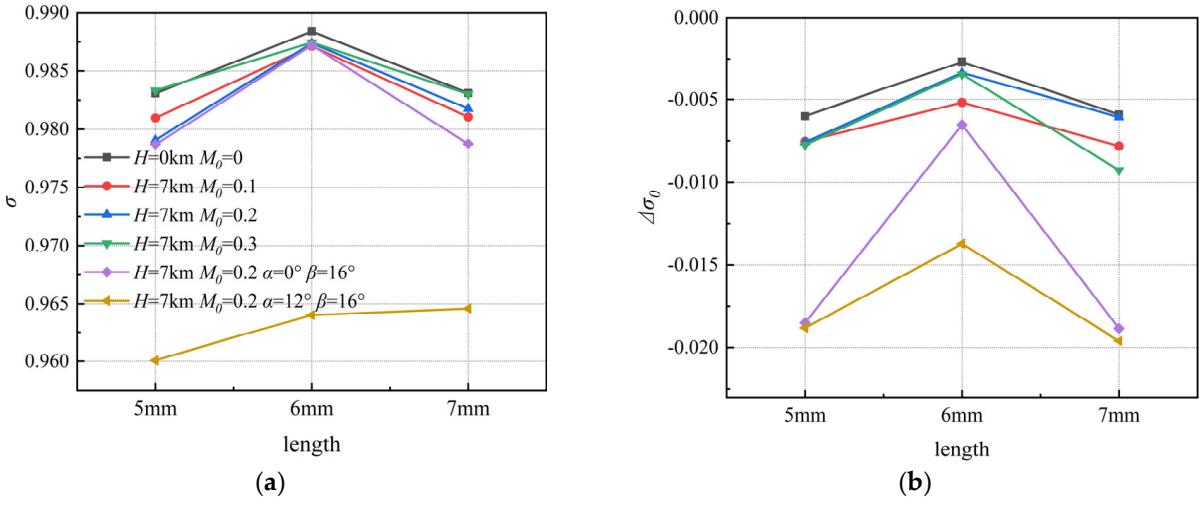

Figure 27. Aerodynamic performance of different grille lengths under various operating conditions. (**a**) the total pressure recovery coefficient, (**b**) the circumferential total pressure distortion index.

It can be concluded from Figure 28 that under symmetric incoming flow conditions with a sideslip angle of 16°, the effect of the grille streamwise length becomes prominent. Specifically, a grille with a streamwise length of 6 mm enables more adequate adjustments to the airflow velocity and pressure distributions, thereby attenuating the intensity of separation vortices. In contrast, an excessively short grille fails to sufficiently mitigate flow disturbances and separation due to insufficient adjustment distance. Meanwhile, an excessively long grille results in an increment in wall friction loss that outweighs the gains from flow field optimization. Both scenarios give rise to an enlarged separation zone and, consequently, a degradation in inlet performance.

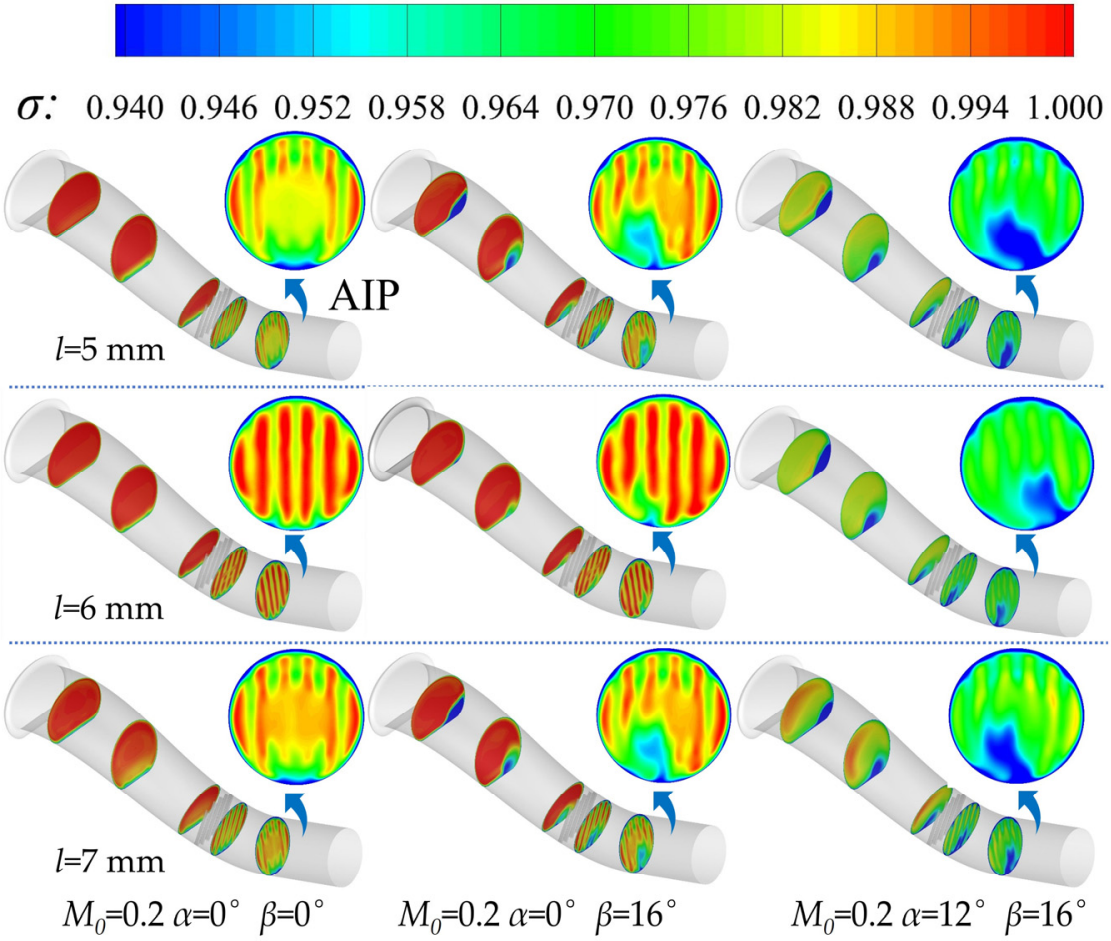

Figure 28. Contour of total pressure recovery coefficient for streamwise cross-sections of inlets with different grille lengths under combined operating conditions.

Figure 29 presents the Mach number, secondary streamlines, and vorticity contours at the AIP section for different grille diameters. It can be observed that the flow field vortex structures formed by excessively long or short grilles are similar; combined with the total pressure contours, the total pressure distribution is also analogous. When the grille length is 7 mm and there is no aerodynamic attitude, small-scale separated vortices with symmetrical and regular distribution are formed. Only the sideslip angle is 16°, and the flow straightening effect of the 6 mm grille is prominent, which can effectively suppress the formation of typical large-scale vortices. Under the coupled effect of angle of attack and sideslip angle, the shear layer disturbance is effectively amplified, leading to the most intense evolution of vortex structures.

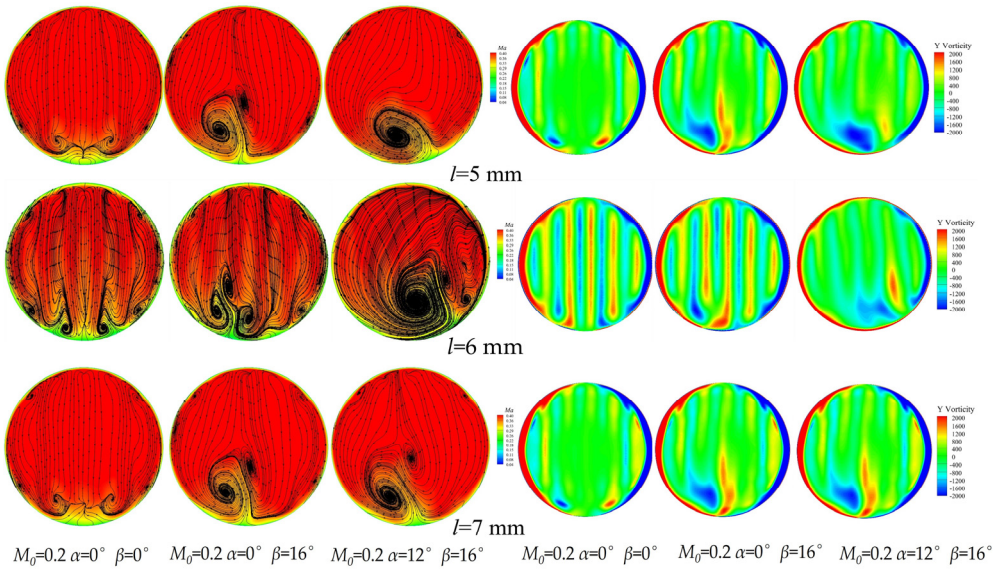

Figure 29. Contours of Mach number, secondary streamlines, and vorticity at the AIP section of different grille lengths under combined operating conditions.

Figure 30 illustrates the flow field characteristics of the symmetry plane for different grille lengths under the same operating conditions. In the absence of flight attitudes, although the S-shaped curved flow field remains continuous overall, a low-velocity zone initially emerges in the curved section. When subjected to asymmetric incoming flow, the symmetry of the flow field deteriorates rapidly, with the low-velocity zone expanding continuously. An excessively short grille length fails to effectively restrict the accumulation of low-velocity flow under complex operating conditions. Conversely, an excessively long grille length leads to increased flow resistance and enhanced energy dissipation, which outweigh the benefits of flow field optimization and instead undermine the smoothness of the flow field. Similarly, under a sideslip angle, both long and short grilles induce high-velocity airflow at the lip, which alleviates the adverse pressure gradient and thereby enhances the wall-attaching capacity of the boundary layer. Under the combined angle condition, however, the 7 mm grille is overly long, resulting in increased drag force, reduced airflow kinetic energy upstream of the grille, localized flow turbulence at the lower lip, and further intensification of flow separation.

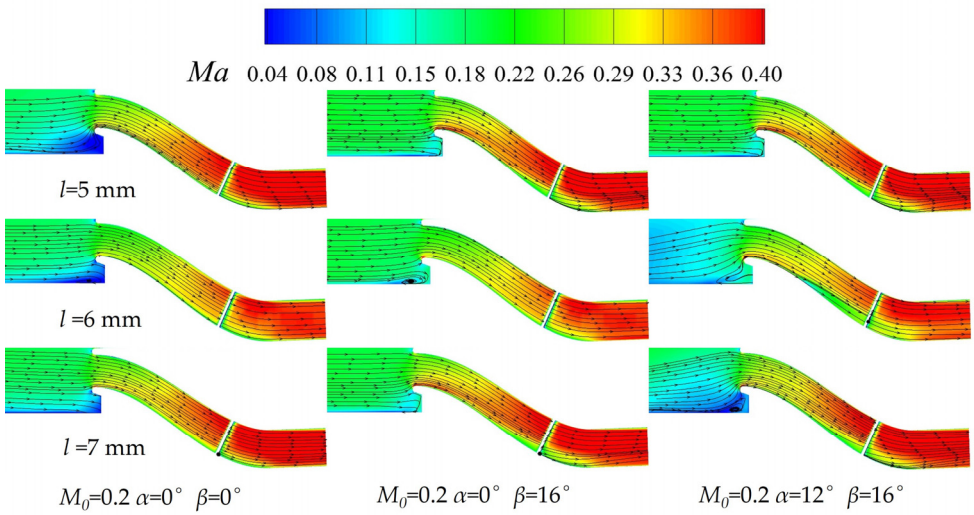

Figure 30. Contour of Mach number and secondary streamlines on the symmetry planes of different grille lengths under combined operating conditions.

Ultimately, in the optimal design of the inlet grille, the I-shaped grille is taken as the optimization object, and it is determined that the configuration with a number of 5, a diameter of 4 mm, and a length of 6 mm exhibits the best aerodynamic performance.

4. Conclusions

Focusing on the integrated UAV, S-shaped inlet, and grille model, this study conducts a numerical simulation study on aerodynamic performance. It places emphasis on aerodynamic performance parameters such as the total pressure recovery coefficient σ and the circumferential total pressure distortion index $\Delta\sigma_0$, and the swirl distortion index.

(1) The grille can effectively improve the circumferential total pressure distortion and swirl characteristics of the UAV S-shaped inlet, but it leads to a decrease in the total pressure recovery coefficient, with Configuration 2 outperforming Configuration 1. Except under extreme conditions of a large angle of attack and large sideslip angle, the swirl distortion index of Configuration 2 is almost zero, so the I-shaped grille has better adaptability than the cross-shaped grille.

(2) As the freestream Mach number increases, the total pressure recovery performance of the baseline configuration and Configuration 1 is slightly improved due to the enhanced ram effect of the inlet airflow, whereas that of Configuration 2 deteriorates. Additionally, the circumferential total pressure distortion of Configuration 1 remains relatively stable, while Configuration 2 shows significant differences. This demonstrates that Configuration 1 has strong adaptability at 7 km altitude without a flight attitude.

(3) An increase in the sideslip angle to 16° results in a significant negative impact on the overall performance of the inlet. Furthermore, the increase in sideslip angle has a more significant impact on Configuration 1 than on Configuration 2, as well as increases the swirl distortion index. Under extreme aerodynamic attitudes, it is necessary to adopt a collaborative matching design between the grille and the inlet to avoid the risk of performance degradation.

(4) Based on the optimal design of Configuration 2, there exists an optimal combination of grille parameters. Except under conditions of large angles of attack and sideslip, the aerodynamic performance of the inlet first improves and then deteriorates with increases in grille number, diameter, and length. Specifically, the configuration with 5 grille rows, a 4 mm diameter, and a 6 mm length achieves an optimal balance between flow regulation and drag suppression.

Author Contributions: Conceptualization, D.L.; Methodology, S.Y., J.R., and Z.W.; Formal analysis, Z.W. (Zhenlong Wu); Investigation, J.R. and S.Y.; Data curation, S.Y.; Writing—original draft, S.Y.; Writing—review and editing, Z.W. (Zhenlong Wu); Visualization, L.Y. (Liming Yang); Supervision, Z.W. (Zhenlong Wu) and M.S. (Mingshuang Ming); Project administration, Z.W. (Zhenlong Wu) and H.T.; Funding acquisition, H.T. All authors have read and agreed to the published version of the manuscript.

Funding: This research received no external funding.

Data Availability Statement: The data presented in this study are available on request from thecorresponding author.

Conflicts of Interest: Author Dongpo Li was employed by the company AVIC (Chengdu) Unmanned Aerial Vehicle System Co., Ltd. The remaining authors declare that the research was conducted in the absence of any commercial or financial relationships that could be construed as a potential conflict of interest.

Nomenclature

AIP	Aerodynamic Interface Plane
UAV	Unmanned Aerial Vehicle
D	Diameter of AIP
d	Grille diameter
l	Grille length
$y+$	Wall Y-plus
RANS	Reynolds-averaged Navier–Stokes
SST	Shear Stress Transport
σ	Total pressure recovery coefficient
$\Delta\sigma_0$	Circumferential total pressure distortion index
P_0	Freestream static pressure
V_0	Tangential velocity
Vy	Axial velocity
θ	Swirl angle
M_0	Mach Number of Freestream
α	Angle of attack
β	Sideslip of Angle
H	Flight Altitude
MFR	Mass flow rate
TP	Total Pressure of Freestream
TT	Total Temperature of Freestream
CFD	Computational Fluid Dynamics
P	Wall static pressure
$R_{\theta,abs7}$	Swirl distortion index

References

1. Lei, L.; Fu, C.; Kun, L.; Huachen, P.; Huawei, Q.; Fang, W.; Maoying, Z.; Xiaoqing, T. Blowing–suction control in S-shaped inlet and its impact on fan-stage performance. *AIAA J.* **2019**, *57*, 3954–3968. [CrossRef]
2. Shi, Z.Y.; Wu, Z.L.; Tan, H.J.; Yao, Y.F. Investigation of two-phase flow characteristics of an S-shaped inlet in rain. *Phys. Fluids* **2025**, *37*, 083324. [CrossRef]
3. Xu, Z.; Gao, R.; Da, X. Assessment and measurement of total pressure distortion based on five-hole-probe for S-shaped inlet. *J. Exp. Fluid Mech.* **2018**, *32*, 78–86.
4. Burrows, T.J.; Vukasinovic, B.; Glezer, A.; Lakebrink, M.T.; Mani, M. Experimental and numerical investigation of active flow control of a serpentine diffuser. *AIAA J.* **2021**, *59*, 607–620. [CrossRef]
5. Wang, K.; Liu, L.; Huang, H.X.; Tan, H.J.; Tang, X.B.; Zheng, G.J. Behavior of flow distortion within a boundary layer ingestion inlet. *Aerosp. Sci. Technol.* **2024**, *146*, 108947. [CrossRef]
6. Ming, L.; Wu, Y.; Yang, Z.; Zhu, Z.; Ouyang, H.; Li, L. Large eddy simulation investigation of S-shaped intake distortion and swirl characteristics. *Aerosp. Sci. Technol.* **2023**, *141*, 108578. [CrossRef]
7. Wang, S.; Zhang, M.; Du, J.; Ba, D.; Nie, C.; Wang, Y. Numerical simulation and prediction using neural network for internal flow field and outlet distortion contour of S-shape inlet ducts. In Proceedings of the Turbo Expo: Power for Land, Sea, and Air, London, UK, 24–28 June 2024.
8. Sadatpour, S.H.; Madadi, A.; Ahadian, R. Numerical optimization of S-shaped intake performance using special cross-sectional profiles. *Thermophys. Aeromechanics* **2022**, *29*, 689–702. [CrossRef]
9. Huang, H.; Shu, S.; Hang, Y.; Tan, H.; Lin, Z.; Li, Z.; Wang, K. Recent progress in subsonic S-shaped inlets. *J. Propuls. Technol.* **2020**, *41*, 2641–2653.
10. Nie, Y.; Li, B.K.; Yang, X.X.; Xie, Y.P.; Zhang, H.Y. Aerodynamic behaviour of ice-debris inside dorsal S-shaped inlet based on overset mesh technology. *Aeronaut. J.* **2025**, *129*, 2497–2522. [CrossRef]
11. Siquig, A. *Impact of Icing on Unmanned Aerial Vehicle (UAV) Operations*; Naval Environmental Prediction Research Facility Report; Naval Environmental Prediction Research Facility: Monterey, CA, USA, 1990.
12. Muhammad, M.; Virk, M.S. Ice accretion on fixed-wing unmanned aerial vehicle—A review study. *Drones* **2022**, *6*, 86. [CrossRef]
13. Villeneuve, E.; Samad, A.; Volat, C.; Béland, M.; Lapalme, M. Experimental investigation of icing effects on a hovering drone rotor performance. *Drones* **2022**, *6*, 345. [CrossRef]

14. Liu, Y.; Li, L.; Chen, W.; Tian, W.; Hu, H. An experimental study on the aerodynamic performance degradation of a UAS propeller model induced by ice accretion process. *Exp. Therm. Fluid Sci.* **2019**, *102*, 101–112. [CrossRef]
15. Lin, Y.; Chen, H.; Wang, G.; Liu, A. Recent progress in preparation and anti-icing applications of superhydrophobic coatings. *Coatings* **2018**, *8*, 208. [CrossRef]
16. Rekuviene, R.; Saeidiharzand, S.; Mažeika, L.; Samaitis, V.; Jankauskas, A.; Sadaghiani, A.K.; Gharib, G.; Muganlı, Z.; Koşar, A. A review on passive and active anti-icing and de-icing technologies. *Appl. Therm. Eng.* **2024**, *250*, 123474. [CrossRef]
17. Hann, R.; Johansen, T.A. *Unsettled Topics in Unmanned Aerial Vehicle Icing*, 1st ed.; SAE International: Warrendale, PA, USA, 2020; pp. 16–18.
18. Hann, R.; Enache, A.; Nielsen, M.C.; Stovner, B.N.; van Beeck, J.; Johansen, T.A.; Borup, K.T. Experimental heat loads for electrothermal anti-icing and de-icing on UAVs. *Aerospace* **2021**, *8*, 83. [CrossRef]
19. Rumpf, R.L.; Shippen, W.B. *Comparison of Aerogrids and Punched Plates for Smoothing Flow from Short Annular Diffusers*; Technical Report, NASA CR-120960; NASA: Washington, DC, USA, 1972.
20. Chiccine, B.G.; Abdalla, K.L. *Experimental Investigation of Expanded Duct Sections and Screens for Reducing Flow Distortions at Subsonic Flows*; Technical Report, NASA-MEMO-1-9-59E; NASA: Washington, DC, USA, 1959.
21. Piercy, T.G.; Klann, J.L. *Experimental Investigation of Methods of Improving Diffuser-Exit Total-Pressure Profiles for Side-Inlet Model at Mach Number 3.05*; Technical Report, NASA-RM-E55F24; NASA: Washington, DC, USA, 1955.
22. Pomposo, J.A.; Rodríguez, J.; Grande, H. Polypyrrole-based conducting hot melt adhesives for EMI shielding applications. *Synth. Met.* **1999**, *104*, 107–111. [CrossRef]
23. Das, N.C.; Khastgir, D.; Chaki, T.K.; Chakraborty, A. Electromagnetic interference shielding effectiveness of carbon black and carbon fibre filled EVA and NR based composites. *Compos. Part A Appl. Sci. Manuf.* **2000**, *31*, 1069–1081. [CrossRef]
24. Menter, F.R. Two-equation eddy-viscosity turbulence models for engineering applications. *AIAA J.* **1994**, *32*, 1598–1605. [CrossRef]
25. Huang, H.X.; Tan, H.J.; Lin, Z.K.; Li, Z.J.; Sun, S.; Chen, H.; Xiao, Z.X. Flowfield of a helicopter submerged inlet with power output shaft. *Acta Mech. Sin.* **2021**, *37*, 156–168. [CrossRef]
26. Sun, S.; Tan, H.J.; Wang, C.X. Submerged inlet performance enhancement using a unique bump-shaped vortex generator. *J. Propuls. Power* **2016**, *32*, 1275–1280. [CrossRef]
27. Wu, Z.L.; Shi, Z.Y.; Sun, S.; Tan, H.J. Two-phase flow characteristics inside a serpentine inlet in heavy rain. *Phys. Fluids* **2025**, *37*, 023313. [CrossRef]
28. Ren, J.; Wu, Z.; Tan, H.; Wang, Z.; He, X.; Li, D.; Zhou, Y. Experimental study of the aerodynamic performance and flow characteristics of an integrated UAV inlet with double 90° bends. *Aerospace* **2024**, *11*, 593. [CrossRef]

Disclaimer/Publisher's Note: The statements, opinions and data contained in all publications are solely those of the individual author(s) and contributor(s) and not of MDPI and/or the editor(s). MDPI and/or the editor(s) disclaim responsibility for any injury to people or property resulting from any ideas, methods, instructions or products referred to in the content.